Journal of Extracellular Vesicles

RESEARCH ARTICLE OPEN ACCESS

Metabolically Engineered Extracellular Vesicles Released From a Composite Hydrogel Delivery System Regulate the Microenvironment for Periprosthetic Osteolysis Treatment

Chenchen Wang[1,2] | Jiang Ju[3] | Chao Fu[3] | Bingbo Bao[1] | Tianhui Ren[3] | Yanan Li[2] | Yuan Wang[2] | Sheng Han[2] | Yuan Wang[2] | Xuan Huang[4] | Hongxing Hu[1] | Xianyou Zheng[1]

[1]Department of Orthopedic Surgery, Shanghai Sixth People's Hospital Affiliated to Shanghai JiaoTong University School of Medicine, Shanghai, China | [2]School of Chemical and Environmental Engineering, Shanghai Institute of Technology, Shanghai, China | [3]School of Chemistry and Chemical Engineering, Key Laboratory of Thin Film and Microfabrication Technology (Ministry of Education), Shanghai Jiao Tong University, Shanghai, China | [4]Department of Orthopedics, The First Affiliated Hospital of Naval Military Medical University, Shanghai, China

Correspondence: Sheng Han (hansheng654321@sina.com) | Xuan Huang (11791709@qq.com) | Hongxing Hu (huhongxing0422@163.com) | Xianyou Zheng (zhengxianyou@126.com)

Received: 1 February 2025 | **Revised:** 22 April 2025 | **Accepted:** 8 May 2025

Funding: This study was supported by Basic Medical Research Foundation of Naval Medical University (2023PY20, 2023MS022). National Natural Science Foundation of China (Grant 82372388, 82172421). 'ChenGuang' project (22CGA75) supported by Shanghai Municipal Education Commission and Shanghai 'Science and Technology Innovation Action Plan' Morning Star Cultivation (Sailing Program 22YF1447500) and Collaborative Innovation Center of Fragrance Flavour and Cosmetics.

Keywords: extracellular vesicles | hydrogel | macrophage | periprosthetic osteolysis | titanium alloys

ABSTRACT

Despite remarkable progress in total joint arthroplasty, aseptic loosening of titanium (Ti) alloy persists as a critical clinical challenge due to the poor wear resistance and biological inertness of such implants. Targeting of inflammatory osteolysis and remodelling of the osseointegration environment represent promising therapeutic approaches to address this issue. In this study, we developed a novel engineered extracellular vesicles (EVs) with a tag of dextran sulfate (DS-EVs) via metabolic glycan labelling (MGL)-mediated click chemistry. This targeted delivery of EVs, derived from metabolically engineered stem cells, establishes a new cell-free therapeutic system for periprosthetic osteolysis. DS-EVs demonstrated specific macrophage tropism, effectively reprogramming macrophage polarisation from pro-inflammatory M1 to regenerative M2 phenotypes. This phenotypic shift attenuated osteoclastogenesis while enhancing osseointegration through GPC6/Wnt pathway activation in vitro. Furthermore, we designed a multifunctional 3D titanium alloy scaffold with MXene-PVA composite hydrogel coatings (Ti-PPM scaffold). The multifunctional Ti-PPM composite scaffold, incorporating DS-EVs, provides a robust delivery system for periprosthetic osteolysis. This integrated system exhibits dual advantages of enhanced wear resistance and optimised interfacial adhesion, while enabling controlled EV release to maximize DS-EVs' osseointegration potential in vivo. Collectively, our findings establish DS-EVs as a transformative therapeutic modality for periprosthetic osteolysis through dual modulation of the osseointegration microenvironment and macrophage phenotypic heterogeneity.

This is an open access article under the terms of the Creative Commons Attribution-NonCommercial-NoDerivs License, which permits use and distribution in any medium, provided the original work is properly cited, the use is non-commercial and no modifications or adaptations are made.

© 2025 The Author(s). *Journal of Extracellular Vesicles* published by Wiley Periodicals, LLC on behalf of the International Society for Extracellular Vesicles.

https://doi.org/10.1002/jev2.70098

1 | Introduction

Total joint arthroplasty (TJA) is an effective orthopaedic procedure to reduce pain and restore patient function (Adams et al. 2021; Chen et al. 2023). Aseptic loosening caused by inflammatory osteolysis in periprosthetic tissue is the primary reason for prosthesis failure and the need for revision surgery (Abd-Elaziem et al. 2024). The poor wear resistance and biological inertness of titanium alloy surfaces are key factors contributing to periprosthetic osteolysis (Drees et al. 2007; Wang et al. 2019). However, no effective therapy is currently available for periprosthetic osteolysis. The wear debris generated by the micro-wear of titanium alloy in the vicinity of bone activates inflammatory cytokines and stimulates osteoclast formation, including tumour necrosis factor-alpha (TNF-α), prostaglandin E2 and interleukin-1 (IL-1), which induce inflammatory osteolysis and aseptic loosening of the implant. Therefore, inhibiting inflammatory osteolysis and remodelling the osseointegration environment is a therapeutic strategy to prevent aseptic loosening.

Investigations suggest that macrophages and osteoclast precursor cells (OCPs) exposed to wear debris at the interface between the implant and the surrounding bone may contribute to periprosthetic inflammatory osteolysis (Jiang et al. 2013; Goodman et al. 1998). Macrophages are incredibly malleable cells that exhibit two distinct phenotypes in disease responses: classically activated (M1) and alternatively activated (M2) (An et al. 2024). M1 macrophages are associated with inflammatory responses and increased levels of reactive oxygen species (Hansen et al. 2024). Exposure to IL-4, IL-13 or IL-10 enhances the polarisation of macrophages towards the M2 phenotype, which has anti-inflammatory properties and significant potential to regulate the immune response, induce angiogenesis and promote tissue regeneration (Yang et al. 2024; Feng et al. 2023). Notably, the fundamental mechanism of bone resorption is thought to involve the interaction between macrophages and osteoclasts (Liao et al. 2024). M1 macrophages perform various biological functions in certain pathological conditions, resulting in osteoclast formation and inflammatory bone resorption (Hascoët et al. 2023). Furthermore, restoring the inflammatory microenvironment upon osteolysis by directly shifting macrophage polarisation from M1 to M2 phenotype has recently gained considerable attention. Recent studies have shown that inducing macrophage polarisation to the M2 phenotype can inhibit the maturation and activity of osteoclasts (Liao et al. 2024; Hascoët et al. 2023). Therefore, targeting and repolarising macrophages to M2 phenotype may offer a promising therapeutic strategy for inflammatory osteolysis.

Recent advancements in extracellular vesicles (EVs) as a promising component for cell-free therapy, known for their low immunogenicity and high stability, have shown potential in regulating inflammation and facilitating bone regeneration (Hu et al. 2020, 2022, 2023). Notably, cell-specific delivery of EVs cargo is crucial to achieving EVs efficacy (Bhatta et al. 2023; Liang et al. 2020). However, there are still no effective procedures to surface-edit EVs to target macrophage cells and enhance polarisation efficiency (Wang and Mooney 2020). Theoretically, EVs may incorporate amine-bearing proteins inherited from the originating cell for surface-editing via metabolic glycan labelling (MGL) (Wang and Mooney 2020; Wang et al. 2017). Compared to typical engineering modification techniques that depend on natural surface protein receptors, MGL combined with bio-orthogonal click chemistry shows numerous strong points, such as higher targeting efficiency, less immunogenicity (Wang et al. 2017). The type A scavenger receptor (SR-A) is a macrophage-specific protein that is activated during immune responses. SR-A is a phagocytic and innate immune recognition receptor that play a vital role in innate immunity and inflammatory signaling regulation (Alquraini and El Khoury 2020). As a specific ligand of SR-A, dextran sulfate (DS) can selectively bind to the positively charged residues of SR-A residues (Liu et al. 2021). In this study, we prepared a novel engineering DS-EVs using click chemical technolgy to target macrophages and inhibit inflammatory osteolysis.

Osseointegration is the process through which implants are physically and functionally integrated into the bone tissue network, forming a stable connection (Overmann et al. 2020; Zhou et al. 2023). Hydrogels provide excellent anti-wear properties for titanium alloys in contact with bone by dissipating interface force (Chen et al. 2024; Gao et al. 2023). Notably, hydrogels are considered promising drug delivery material that can be directly integrated into the osseointegration environment (Marquardt et al. 2020; Han et al. 2022). PVA hydrogels are stabilised by interchain hydrogen bonds and hydrophobic interactions, forming lamellar-like network junction knots, whereas an increase in temperature gives rise to the dissociation of hydrogen bonds with ensuing dissolution of the hydrogel (Pedersen et al. 2020). MXene materials have high absorption and photothermal conversion efficiencies for near-infrared (NIR) light (Wu et al. 2011). Herein, we designed a multifunctional 3D titanium alloy scaffold with MXene-PVA composite hydrogel coatings (referred to Ti-PPM scaffold). The hydrogel coated DS-EVs were gradually dissolved by regulating NIR light irradiation, leading to the sustained and stable release of DS-EVs.

In this work, we developed a novel therapeutic strategy for periprosthetic osteolysis based on the novel engineered DS-EVs from metabolic glycan labelling hUCMSCs via MGL-mediated click chemistry (Scheme 1a), Moreover, we constructed a robust delivery system with a multifunctional Ti-PPM composite scaffold, which exhibited desirable wear resistance, excellent interfacial adhesion, and enabled the frequency-controlled release of EVs through NIR light regulation (Scheme 1b), maximising the osseointegration effects of DS-EVs in vivo. DS-EVs targeted macrophages and shifted macrophage polarisation from the M1 to the M2 phenotype, inhibiting osteoclastogenesis and promoting osteogenic differentiation in vitro. Furthermore, transcriptome profiling of BMSCs and RAW cells stimulated by optimised DS-EVs was performed to reveal potential molecular mechanisms (Scheme 1c).

2 | Results

2.1 | Metabolic Glycan Labelling (MGL) of hUCMSCs Generates Chemically Tagged DS-EVs

SR-A is a macrophages-specific protein that is activated in response to inflammation. SR-A receptors contribute to immune regulation and inflammation suppression by facilitating pathogen clearance, limiting pro-inflammatory cytokine

20013078, 2025, 6, Downloaded from https://isevjournals.onlinelibrary.wiley.com/doi/10.1002/jev2.70098 by CochraneChina, Wiley Online Library on [23/06/2025]. See the Terms and Conditions (https://onlinelibrary.wiley.com/terms-and-conditions) on Wiley Online Library for rules of use; OA articles are governed by the applicable Creative Commons License

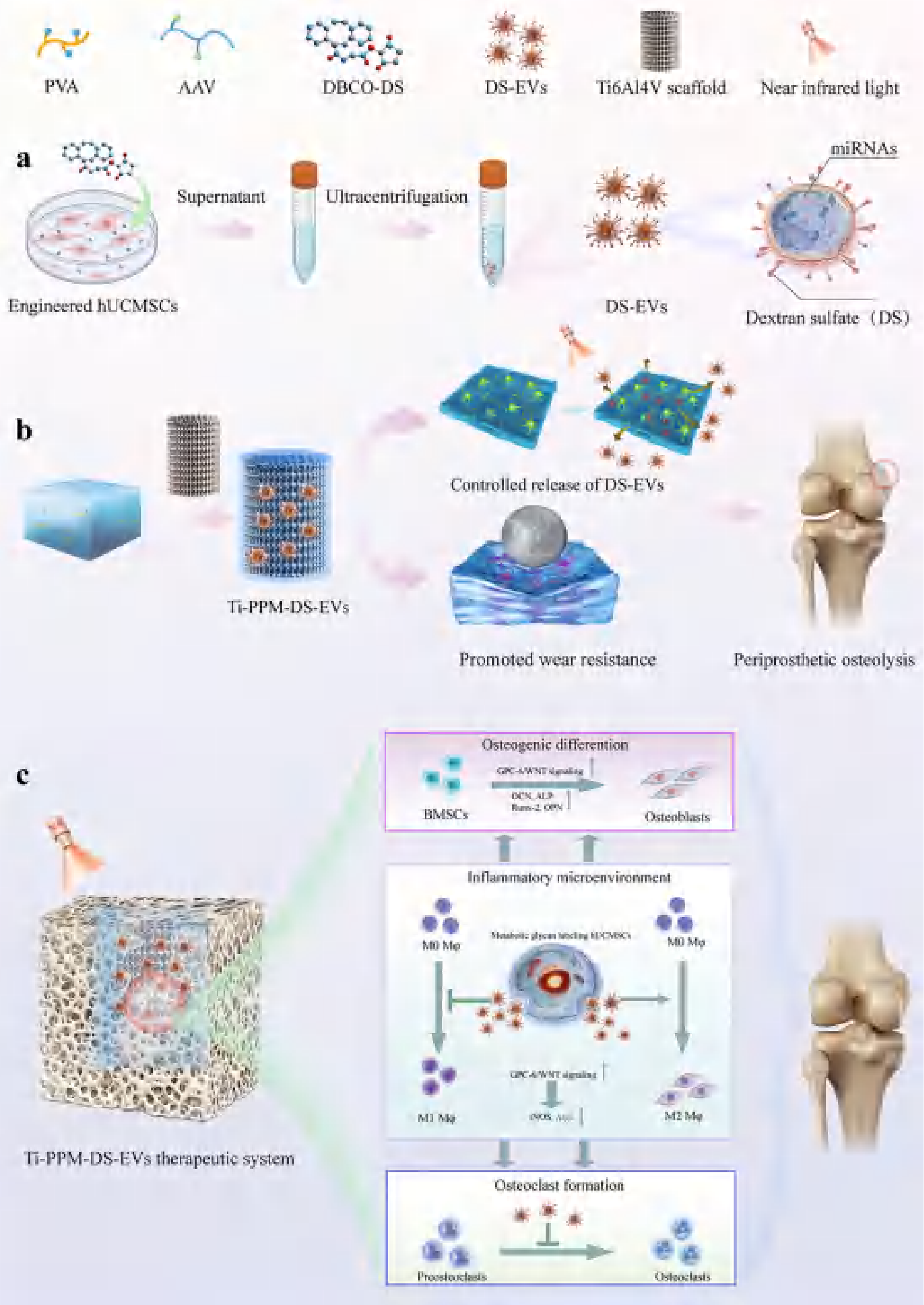

SCHEME 1 | Schematic illustration of MXene-PVA composite hydrogel delivery system with controllable release of metabolic glycan labelling extracellular vesicles enhanced titanium alloy osseointegration.

production, promoting immune tolerance through apoptotic cell clearance, and driving macrophage polarisation towards anti-inflammatory phenotypes. As specific ligands of SR-A, DS can selectively bind to the positive charges on SR-A residues (Liu et al. 2021). We aim to fabricate engineering EVs that specifically target activated macrophages. Firstly, hUCMSCs acquired the azide group through the co-incubation with tetraacetyl N-azidoacetylmannosamine (Ac_4ManAz) for 48 h. Then, the azide group on the surface of hUCMSCs binds to Cy5.5-labelled DBCO-DS via MGL-mediated click chemistry technology (Figure 1a). As shown in Figure 1b,c, the fluorescence intensity of Cy5.5-labelled DBCO-DS on the surface of hUCMSCs was dose-dependent on $Ac_4ManNAz$. Furthermore, EFA1, an early endosome marker, was evaluated by immunofluorescence to observe the time-dependent localisation of Cy5.5-labelled DS (Figure 1d,e). As expected, EFA1 fluorescence signal was observed and co-localised with Cy5.5-labelled DS in the time-dependent manner, indicating the newly generated EVs harboured DS tag. CD63 is a specific marker of EVs and involve in EV biogenesis (Kalluri and LeBleu 2020). CD63 immunofluorescence was performed to observe EV biogenesis after the surface MGL engineering of hUCMSCs using click chemistry. Our results revealed that CD63 (green fluorescence) was co-localised with DS (red fluorescence) 6 h after the surface engineering of

20013078, 2025, 6, Downloaded from https://isevjournals.onlinelibrary.wiley.com/doi/10.1002/jev2.70098 by CochraneChina, Wiley Online Library on [23/06/2025]. See the Terms and Conditions (https://onlinelibrary.wiley.com/terms-and-conditions) on Wiley Online Library for rules of use; OA articles are governed by the applicable Creative Commons License

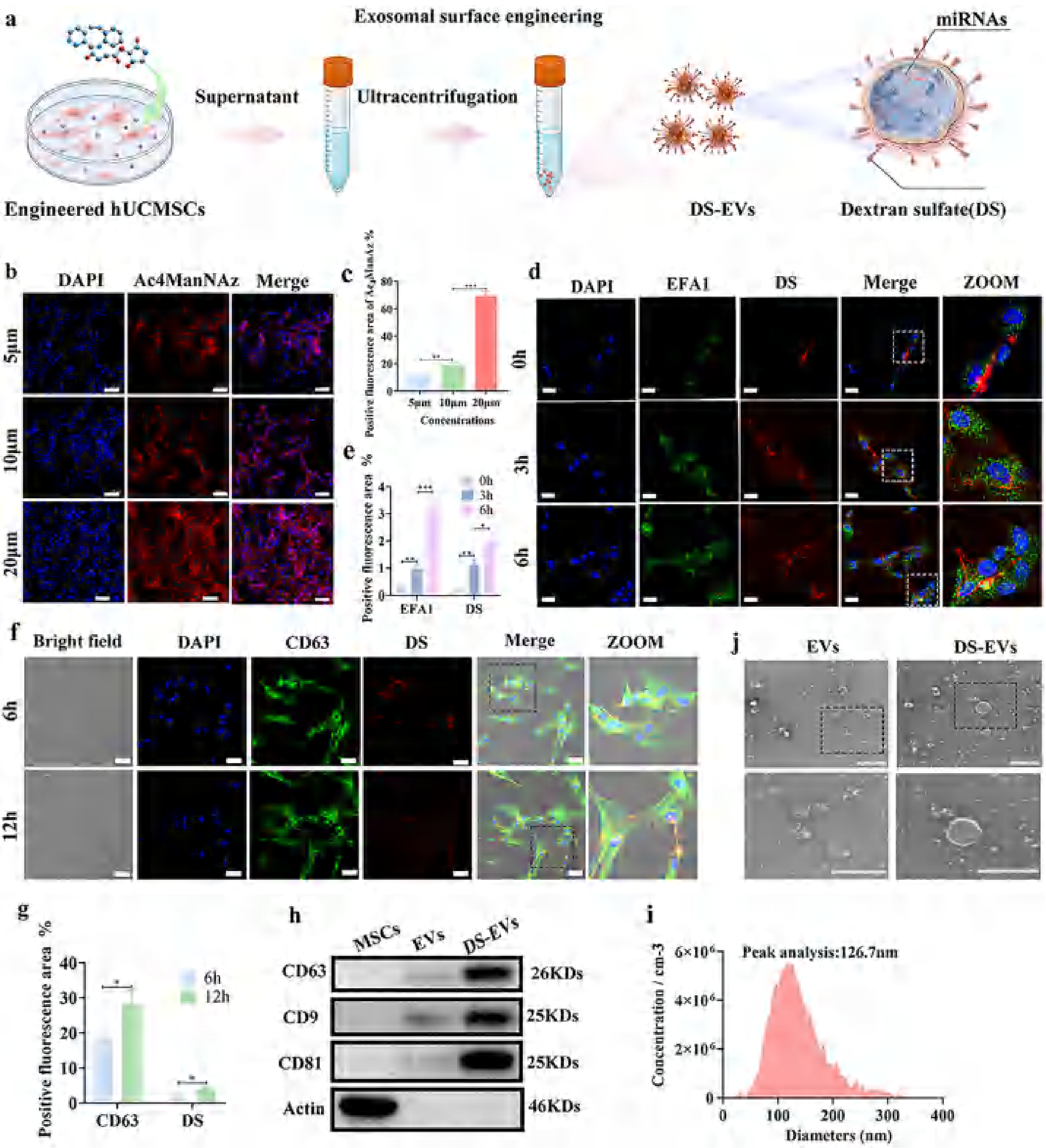

FIGURE 1 | Metabolic glycan labelling (MGL) of hUCMSCs generates chemically tagged DS-EVs. (a) Schematic of exosomal surface engineering. (b) Representative confocal images of DS-modified hUCMSCs at different concentrations of $Ac_4ManNAz$ by efficient click chemistry. hUCMSCs were incubated with Ac_4ManAz for 48 h to obtain the azide group. Then, hUCMSCs labelled with azide group were treated with Cy5.5-labelled dibenzocyclooctyne-conjugated dextran sulfate (DBCO-DS) (10 μM) for 2 h. Scale bar: 100 μm. (c) Quantification of the positive fluorescence area of Ac_4ManAz ($n = 3$, $**p < 0.01$, $***p < 0.001$). (d) Representative confocal images of the early EVs marker EFA1 and Cy5.5-marked DS in the metabolic glycan labelling hUCMSCs at different time points. Scale bar: 20 μm. (e) Positive fluorescence area of EFA1 and Cy5.5-marked DS ($n = 3$, $*p < 0.05$, $**p < 0.01$, $***p < 0.001$). (f) Confocal microscopy images reveal the intracellular colocalisation of CD63 and Cy5.5-marked DS in the hUCMSCs. Scale bar: 20 μm. (g) Positive fluorescence area of CD63 and Cy5.5-marked DS ($n = 3$, $*p < 0.05$, $**p < 0.01$, $***p < 0.001$). (h) Western blot was used to characterise the surface markers of EVs and DS-EVs. (i) Particle size of DS-EVs measured via nanoparticle tracking analysis (NTA). (j) TEM images show the morphology of EVs and DS-EVs. Scale bar: 500 nm.

20013078, 2025, 6, Downloaded from https://isevjournals.onlinelibrary.wiley.com/doi/10.1002/jev2.70098 by CochraneChina, Wiley Online Library on [23/06/2025]. See the Terms and Conditions (https://onlinelibrary.wiley.com/terms-and-conditions) on Wiley Online Library for rules of use; OA articles are governed by the applicable Creative Commons License

hUCMSCs. Moreover, the co-localised fluorescent signal was enhanced after 12 h (Figure 1f,g).

The exosomal surface markers CD81, CD63 and CD9 were expressed in both DS-EVs and EVs (Figure 1h). The average diameter of the DS-EVs was approximately 127.6 nm, and the concentration was 2×10^{11} particles/mL (Figure 1i). Taken together, the above results demonstrate that MGL modification of hUCMSCs was successfully achieved via click chemistry, and DS-EVs were successfully extracted from the conditioned medium without exosomal dysfunction. In addition, TEM was performed to observe the morphological differences between DS-modified EVs and unmodified EVs. Our results showed that both DS-EVs and EVs exhibited a similar double-layered membrane structure, but DS-EVs had a larger diameter of approximately 95 nm compared to EVs (Figure 1j).

2.2 | Construction of Anti-Wear Coating on the 3D Porous Ti6Al4V Scaffolds to Reduce Wear Debris

Surface coating technology has been regarded as an efficacious and straightforward approach to enhance the wear resistance of this titanium alloy. MXene has received widespread attention for improving the tribological properties from the biomedical field (Wang et al. 2024). Moreover, MXene is a promising material for establishing the stimulus responsive drug delivery system due to its high absorption and photothermal conversion efficiency for near-infrared light. We aim to fabricate an anti-wear coating on the 3D porous Ti6Al4V scaffolds to reduce wear debris. Firstly, two-dimensional MXene was synthesised by HF etching, as shown in Figure 2a. The detailed preparation process is provided in the Supporting Information (SI 1.1). The MXene with Layer structure were respectively observed through AFM images (Figure 2b,c) and SEM with EDX (Figure S1). Notably, the prepared MXene was monolayer and multilayer structures with a diameter of approximately 200 nm and thickness of about 5 nm. The corresponding EDX mapping indicated the distribution of Ti element and the removal of Al element, which confirmed the MXene had been successfully prepared. Moreover, through the analysis of Raman and XRD spectrum, the successful synthesis of MXene was also proved in Figure S2.

Hydrogels provide excellent wear resistance to titanium alloys in contact with bone by dissipating interfacial forces (Chen et al. 2024; Gao et al. 2023). PVA/AAC hydrogel had recently attracted increasing attention in tissue engineering due to its injectable and temperature-sensitive properties. We aimed to prepare MXene-PVA/AAC hydrogels to enhance wear resistance of titanium alloys. As shown in Figure 2d, the Raman spectra presented that compared with PVA/AAC hydrogel (PP), the characteristic peaks at 233, 399 and 521 cm appeared on the MXene-PVA/AAC hydrogels (PPM), indicating the presence of MXene in PPM hydrogel. The FTIR spectra of MXene, PP hydrogel and PPM hydrogel are shown in Figure 2e. The curve of MXene exhibited that the absorption peaks of –OH appeared at 3453 and 1655 cm. In the FTIR spectra of PP and PPM hydrogel, the stretching vibration peak of C = O in ester bond at 1700 and 1711 cm were found, implying the reaction between the hydroxyl group of MXene and PVA with the carboxyl group in acrylic acid.

The strain amplitude sweep of the PP and PPM hydrogels were evaluated (Figure 2f). It is significant that the G′ (storage modulus) curve and G″ (loss modulus) curve intersected at a point of 1000%, indicating that when the strain was larger than 1000%, the hydrogel structure was completely broken. Moreover, the G′ and G″ of PPM hydrogels was higher than that of PP, implying the increased cross-linking density of the PPM hydrogel due to the introduction of MXene. Figure S3 showed the variation of storage modulus and loss modulus of PP and PPM hydrogels with frequency. It can be seen from the figure that the storage modulus and the loss modulus of hydrogels increased with the increasing of frequency, and the storage modulus of PP and PPM hydrogels were far greater than that of the loss modulus, demonstrating the excellent energy storage network structure. Compared with PP and PPM hydrogels, the similar trend of G′ and G″ was observed, suggesting the improved network structure stability of PPM hydrogel through doping the MXene sheets (Jafarigol et al. 2021).

The micrographs of titanium scaffolds were shown in Figure S4. And the coating thickness and adhesion strength of Ti-PPM scaffold were evaluated in Figures S5 and S6. As described in the Supporting Information 1.4, the anti-wear properties of Ti, Ti-PP and Ti-PPM samples in SBF lubrication was evaluated. The wear rates results were shown in Figure 2g, with the following sequence: Ti > Ti-PP > Ti-PPM. The corresponding 3D topography of wear scar surfaces of three samples were exhibited in Figure 2h. The remarkable results showed that the PP and PPM hydrogel coating effectively improved the anti-wear properties of titanium alloy scaffold, with the significant reduction (84.9%) of wear rate from PPM coating.

2.3 | DS-EVs Influence Macrophage Polarisation and Suppress Osteoclastogenesis In Vitro

The wear debris generated by micro-wear of titanium alloy in the vicinity of bone is the main cause of inflammatory osteolysis. Macrophages are the main immune cells that activate inflammatory cytokines, including tumour necrosis factor-alpha (TNF-α), and prostaglandin E2, and interleukin-1 (IL-1), thereby regulating the process of inflammatory osteolysis (Yin et al. 2022). To mimic the inflammatory osteolysis microenvironment in vitro, we prepared Ti-PPM wear debris in vitro. RAW 264.7 cells were cultured with DS-EVs following LPS and Ti-PPM wear debris stimulation (Figure 3a). Inducible nitric oxide synthase (iNOS) is a pro-inflammatory cytokine and play an important role in maintaining M1 macrophage phenotype. Immunofluorescence results revealed that EVs and DS-EVs treatment significantly downregulated the expression of iNOS in RAW cells induced by LPS and Ti-PPM wear debris. Notably, DS-EVs are more effective at inhibiting inflammatory microenvironment (Figure 3b,c). CD206 is a marker for an alternative type of activated macrophage known as M2 macrophage (Groenbaek et al. 2015; Nielsen et al. 2020) DS-EVs significantly upregulated the expression of CD206 in RAW cells compared to the EVs (Figure 3d,f), indicating DS-EVs are more effective in skewing macrophage polarisation from M1 to M2 phenotype. Osteoclast formation and activation play a crucial role in inflammatory osteolysis (Kitaura et al. 2020). Trap staining was carried out to further elucidate the function of DS-EVs in modulating osteoclast formation and bone metabolism

20013078, 2025, 6, Downloaded from https://isevjournals.onlinelibrary.wiley.com/doi/10.1002/jev2.70098 by CochraneChina, Wiley Online Library on [23/06/2025]. See the Terms and Conditions (https://onlinelibrary.wiley.com/terms-and-conditions) on Wiley Online Library for rules of use; OA articles are governed by the applicable Creative Commons License

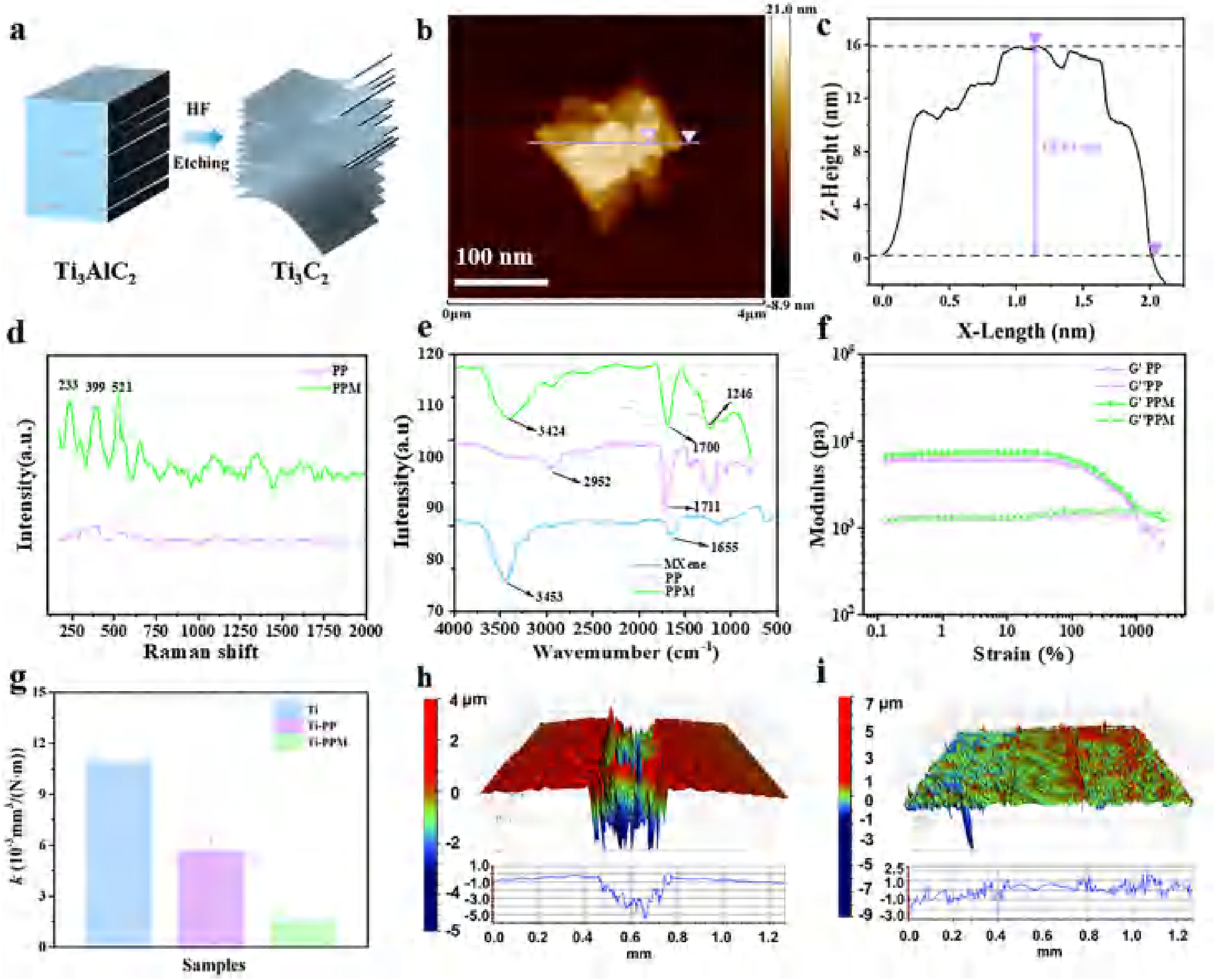

FIGURE 2 | Construction of anti-wear coating on the 3D porous Ti6Al4V scaffolds to reduce wear debris. (a) Fabrication of Ti2C3 MXene. (b and c) AFM images of the Ti2C3 MXene. (d) Raman spectrum of PP and PPM hydrogel. (e) FTIR spectrum of MXene, PP and PPM hydrogel. (f) Strain amplitude sweep test ($\gamma = 0.1\%-1500\%$) at a fixed angular frequency (1 Hz) at 25°C. (g) Wear rates of Ti, Ti-PP and Ti-PPM samples. (h and i) 3D topography of wear scar surfaces of Ti and Ti-PPM samples.

(Figure 3e,g). The receptor activator of nuclear factor κB ligand (RANKL) is an essential factor for osteoclast formation (Kitaura et al. 2020). EVs and DS-EVs inhibited the osteoclastogenesis in RAW cells, whereas DS-EVs showed a more pronounced effect on suppressing osteolysis by inhibiting inflammatory microenvironment (Figure 3h-j), repolarising macrophages from M1 to M2 type and suppressing osteoclast formation.

2.4 | DS-EVs Are Conducive to Promote Osteogenic Differentiation of BMSCs In Vitro

Encouraging the formation of osseointegration around bone implants and reducing the occurrence of periprosthetic osteolysis are crucial for enhancing bone implants fixation (Li et al. 2016). To further investigate the osteogenic role of DS-EVs on BMSCs in the osteolysis microenvironment in vitro, BMSCs were co-incubated with DS-EVs in the presence of Ti-PPM wear debris (Figure 4a). The fluorescence micrograph (Figure 4b) showed that PKH-26-labelled EVs and DS-EVs (red fluorescence) were gradually internalised by BMSCs, with nuclei were stained in blue by DAPI. As illustrated in Figure 4c, both EVs and DS-EVs significantly promoted the proliferation of BMSCs on the 3 and 7 days, whereas DS-EVs exhibited more pronounced effect in enhancing BMSCs viability. Furthermore, the osteogenic effect of DS-EVs on BMSCs was investigated by ALP activity and calcium deposition assays. Compared to EVs treatment, DS-EVs treatment significantly enhanced ALP activity and showed higher ALP positive area, as well as higher detection of calcium deposits assessed by ARS staining (Figure 4d). Additionally, immunofluorescent images from confocal laser microscopy revealed that osteocalcin (OCN) production was significantly enhanced in the BMSCs treated with DS-EVs plus Ti-PPM (Figure 4e,f). Osteopontin (OPN) is one of the more abundant non-collagenous proteins in the bone matrix produced by osteoblasts and osteoclasts, which can effectively stimulate osteoclastogenic and resorptive activity in mature osteoblasts (Simonet et al. 1997; Udagawa et al. 2021). DS-EVs upregulated the expression of OPN and Runt-related transcription factor 2 protein under Ti-PPM wear debris stimulation (Figure 4g). Consistently, DS-EVs were more favourable

20013078, 2025, 6, Downloaded from https://isevjournals.onlinelibrary.wiley.com/doi/10.1002/jev2.70098 by CochraneChina, Wiley Online Library on [23/06/2025]. See the Terms and Conditions (https://onlinelibrary.wiley.com/terms-and-conditions) on Wiley Online Library for rules of use; OA articles are governed by the applicable Creative Commons License

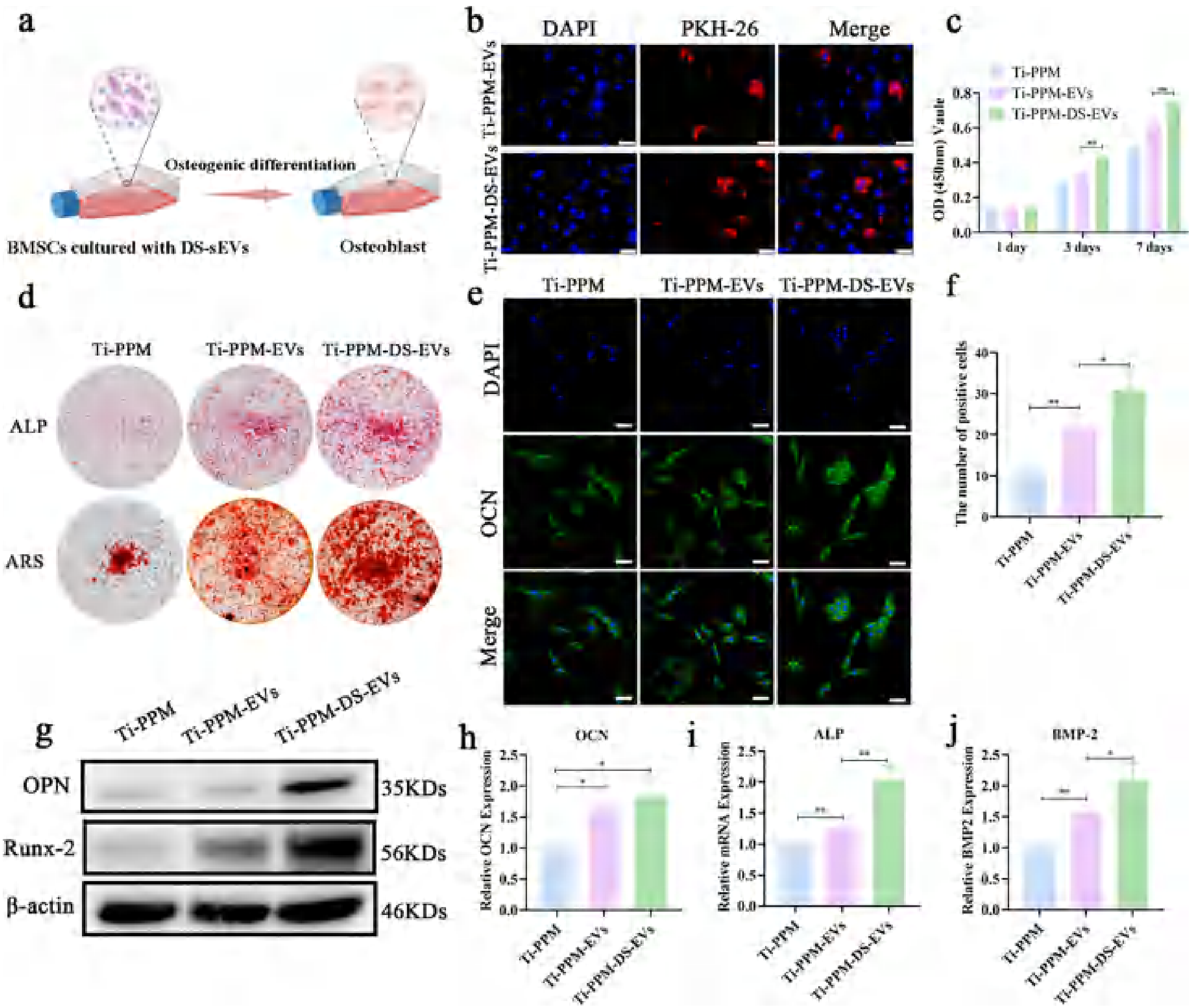

FIGURE 3 | DS-EVs influence macrophage polarisation and suppress osteoclastogenesis in vitro. (a) Mode pattern of macrophage polarisation from M1 to M2 phenotype induced by DS-EVs stimulation. (b) Immunofluorescence staining of iNOS in RAW 264.7 cells. Ti-PPM-EVs and Ti-PPM-DS-EVs groups respectively represent RAW 264.7 cells were treated with EVs or DS-EVs in the presence of Ti-PPM wear debris (2 mg/mL) and lipopolysaccharide (LPS, 500 ng/mL). Scale bar: 100 µm. (c) Quantitative analysis of iNOS-positive cells. Immunofluorescence positive cells were analysed using Image J software ($n = 3$, $**p < 0.01$, $***P < 0.001$). (d) Immunofluorescence staining of CD206 in RAW 264.7 cells. Ti-PPM-EVs and Ti-PPM-DS-EVs groups respectively represent RAW 264.7 cells were treated with EVs or DS-EVs in the presence of Ti-PPM wear debris and LPS. Scale bar: 100 µm. (e) Representative photograph of tartrate-resistant acid phosphatase (TRAP) staining. Ti-PPM-EVs and Ti-PPM-DS-EVs groups respectively represent RAW 264.7 cells were treated with EVs or DS-EVs in the presence of Ti-PPM wear debris, LPS and RANKL. (f) Quantitative analysis of CD206-positive cells. Immunofluorescence positive cells were analysed by Image J software ($n = 3$, $***p < 0.001$). (g) Quantitative analysis of TRAP-positive areas ($n = 3$, $**p < 0.01$, $***p < 0.001$). (h-j) qPCR analysis of Arg1, CD206 and MMP-9 gene expression respectively ($n = 3$, $***p < 0.001$). Data was presented as mean ± SD of three number of replicates. *t*-test was applied to each group in order to compare mean beta values.

to enhance the mRNA expression levels of osteogenesis-related genes such as ALP, bone morphogenetic protein-2(BMP-2), osteocalcin (OCN) than EVs treatment (Figure 4h-j). At last, the above results indicated that DS-EVs were conducive to inhibit osteolysis and promote osseointegration in vitro.

2.5 | Transcriptome Profiling of BMSCs and RAW Cells Stimulated by Optimised DS-EVs

Transcriptome profiling of DS-EVs treated BMSCs (Figure 5a-f) and RAW 264.7 cells (Figure 5g-j) was performed to investigate the potential mechanism of DS-EVs mediated osseointegration in vitro. Volcano plots showed differentially expressed genes (DEGs) between Ti-PPM and Ti-PPM-DS-EVs groups (Figures 5a and S7). In BMSCs, 1468 genes were upregulated and 1005 were downregulated; in RAW 264.7 cells, 1069 genes were upregulated and 1490 were downregulated ($p < 0.05$, log2 fold change >1). A detailed analysis of KEGG pathway enrichment ($p < 0.05$, $\log_2$ fold change >1) revealed that differentially expressed genes (DEGs) were predominantly associated with Hippo and Wnt signalling pathways (Figure 5b,g). In particular, Wnt signalling pathway executes an indispensable performance in skeletal homeostasis and bone remodelling (Canalis 2013; Vlashi et al. 2023). KEGG relation

20013078, 2025, 6, Downloaded from https://isevjournals.onlinelibrary.wiley.com/doi/10.1002/jev2.70098 by CochraneChina, Wiley Online Library on [23/06/2025]. See the Terms and Conditions (https://onlinelibrary.wiley.com/terms-and-conditions) on Wiley Online Library for rules of use; OA articles are governed by the applicable Creative Commons License

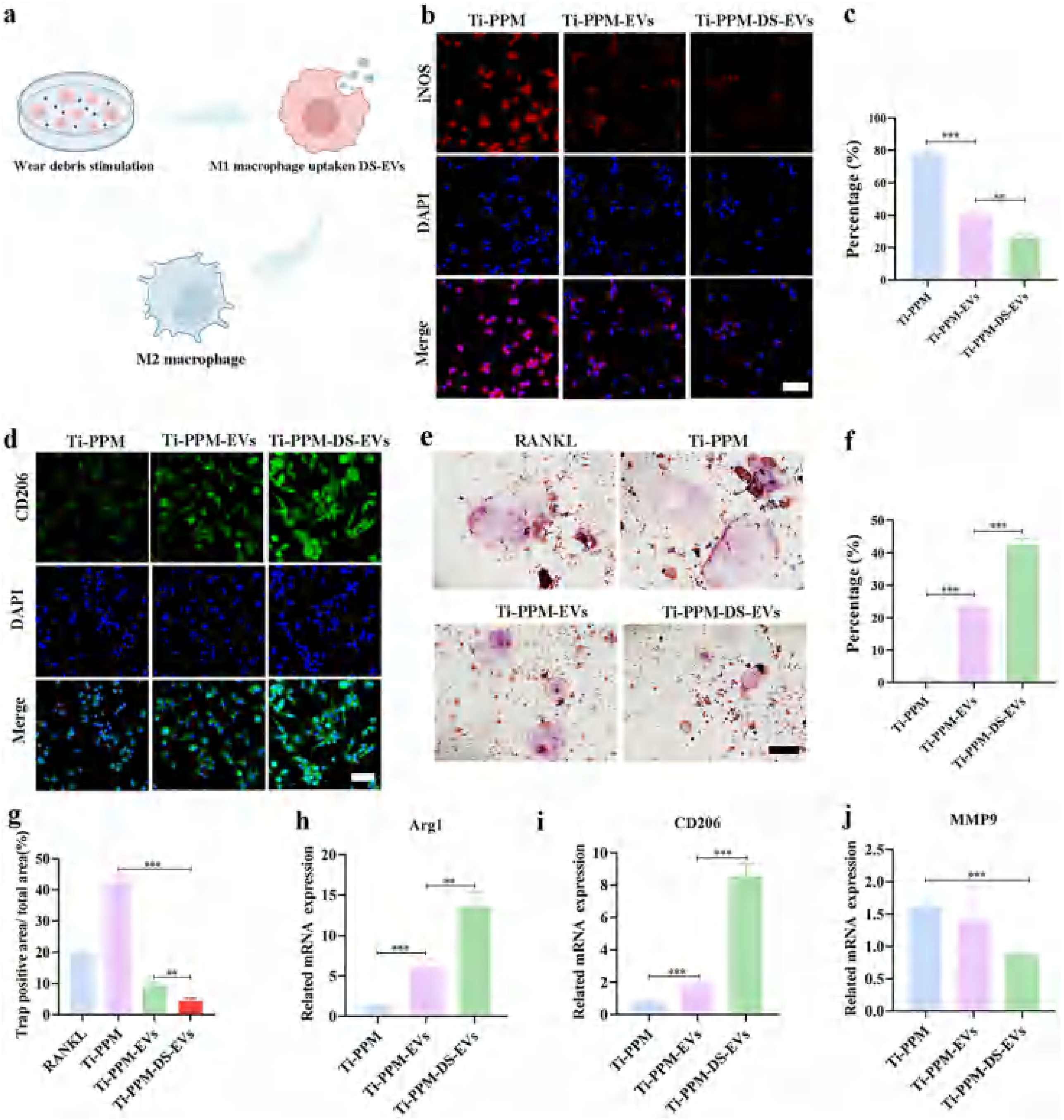

FIGURE 4 | DS-EVs are conducive to promote osteogenic differentiation of BMSCs in vitro. (a) Scheme of the osteogenic differentiation of BMSCs stimulated by DS-EVs. (b) Representative fluorescence micrograph of PKH-26 (red)-labelled DS-EVs internalised by BMSCs. Scale bar: 20 µm. (c) CCK-8 assay of BMSCs cultured with DS-EVs. $^{**}p < 0.01$. Ti-PPM-EVs and Ti-PPM-DS-EVs group respectively represent BMSCs were treated with EVs or DS-EVs in the presence of Ti-PPM wear debris. (d) Alkaline phosphatase (ALP) activity and Alizarin Red S (ARS) staining of BMSCs. (e) Immunofluorescent of OCN in BMSCs. Scale bar: 100 µm. (f) Quantitative analysis of OCN positive cells. Immunofluorescence positive cells were analysed by Image J software ($n = 3$, $^{*}p < 0.05$, $^{**}p < 0.01$). (g) The protein levels of OPN and Runx-2 in BMSCs were analysed by western blotting. (h-j) The osteogenic-related gene of BMSCs was measured via the qPCR, including OCN, ALP and BMP-2. $^{*}p < 0.05$, $^{**}p < 0.01$. Data was presented as mean ± SD of three number of replicates. *t*-test was applied to each group in order to compare mean beta values.

networks and heatmap distribution revealed that Glypican 6 (GPC6) was one of the DEGs and was closely associated with Wnt signalling pathway, indicating GPC6 may be the key gene of the Wnt signalling pathway (Figure 5c,e,h). GPC6 is a member of the GPC family and is implicated in the control of cell growth and cell division (Capurro et al. 2017). Gene ontology (GO) cellular components and molecular function analysis based on DEGs revealed that extracellular matrix (ECM) and collagen-contained ECM was different between the Ti-PPM and Ti-PPM-DS-EVs groups, indicating that DS-EVs may mediate osseointegration by promoting ECM regeneration (Figure 5d,i). Moreover, Wnt signalling pathway was altered in gene set enrichment analysis

20013078, 2025, 6, Downloaded from https://isevjournals.onlinelibrary.wiley.com/doi/10.1002/jev2.70098 by CochraneChina, Wiley Online Library on [23/06/2025]. See the Terms and Conditions (https://onlinelibrary.wiley.com/terms-and-conditions) on Wiley Online Library for rules of use; OA articles are governed by the applicable Creative Commons License

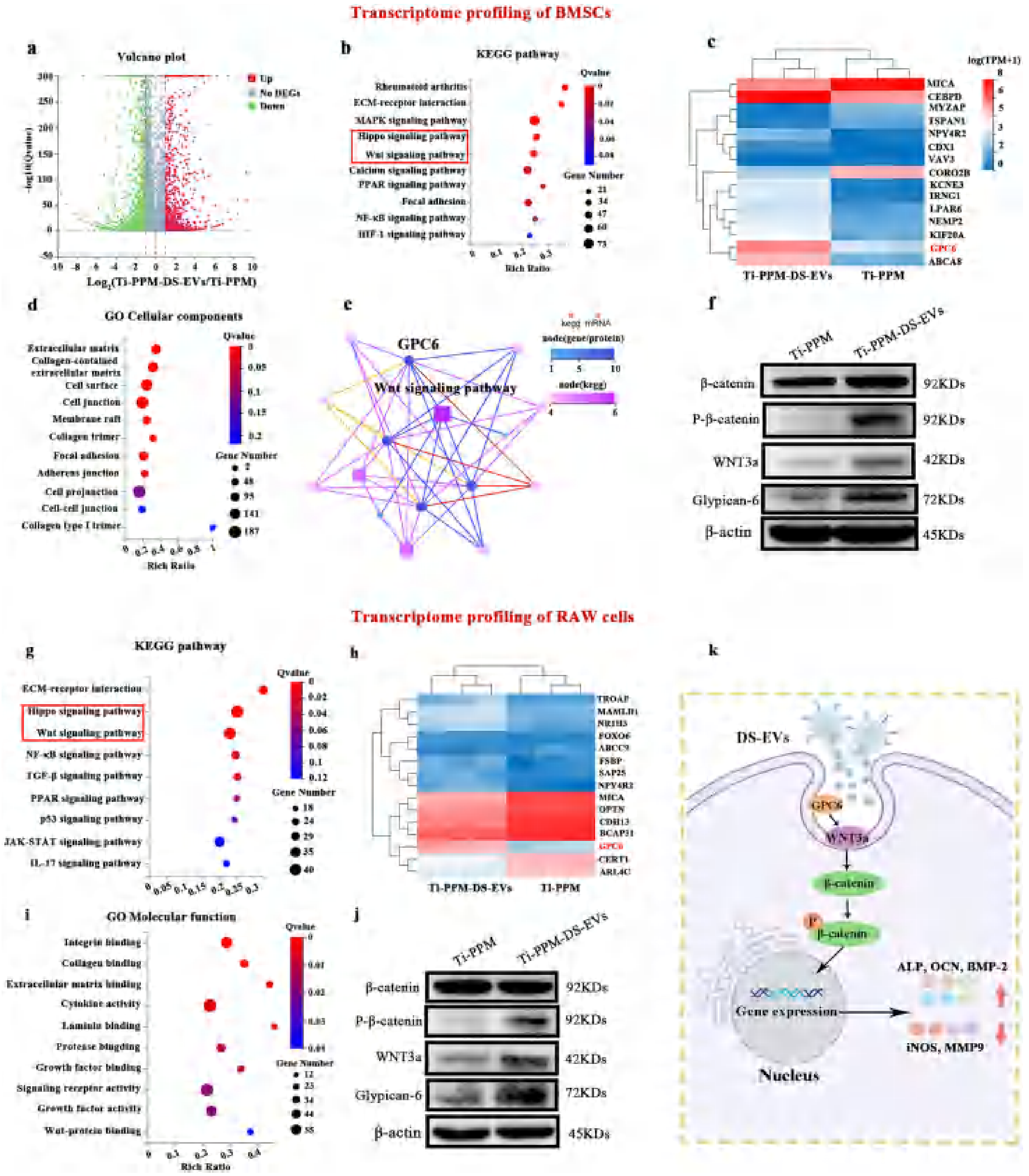

FIGURE 5 | Transcriptome profiling of optimised DS-EVs regulates function and mechanism of BMSCs and RAW cells. (a) The volcano diagram of Ti-PPM-DS-EVs and Ti-PPM group based on transcriptome profiling of BMSCs. (b) KEGG pathway enrichment analysis based on DS-EVs regulated significant target genes. (c) The heatmap distribution of DS-EVs regulating significant target genes. Ti-PPM-DS-EVs group respectively represent BMSCs were treated with DS-EVs in the presence of Ti-PPM wear debris. (d) Graphene oxide-interactive (GO) cellular contents analysis for the cellular component of differential target genes. (e) KEGG relation networks based on DS-EVs regulated significant target genes. (f) The related proteins of GPC6/Wnt signalling pathway in BMSCs measured by western blot. (g) KEGG pathway enrichment analysis based on DS-EVs regulated significant target genes. (h) The heatmap distribution of DS-EVs regulating significant target genes. Ti-PPM-DS-EVs group respectively represent RAW264.7 cells were treated with DS-EVs in the presence of Ti-PPM wear debris and LPS. (i) GO molecular function analysis of differential target genes. (j) DS-EVs inhibit osteolysis and promote bone osseointegration in vitro by activating GPC6/Wnt signalling pathway. (k) A schematic representation illustrates the roles of DS-EVs in inhibit osteolysis and promote bone osseointegration.

20013078, 2025, 6, Downloaded from https://isevjournals.onlinelibrary.wiley.com/doi/10.1002/jev2.70098 by CochraneChina, Wiley Online Library on [23/06/2025]. See the Terms and Conditions (https://onlinelibrary.wiley.com/terms-and-conditions) on Wiley Online Library for rules of use; OA articles are governed by the applicable Creative Commons License

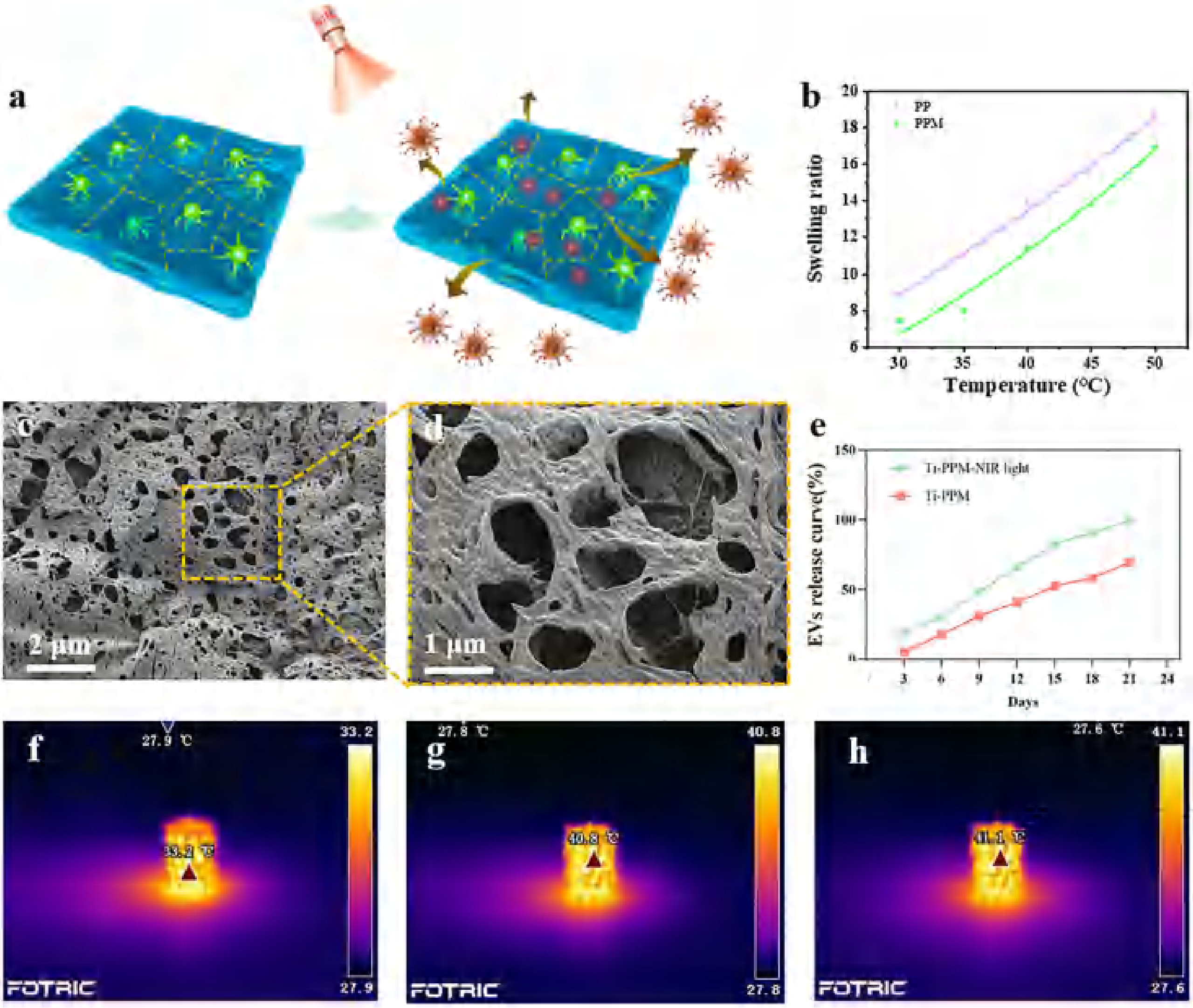

FIGURE 6 | Characterisation of extended release of DS-EVs in Ti-PPM composite scaffolds. (a) Scheme of extended release of DS-EVs in Ti-PPM composite scaffolds. (b) Swelling properties of PP and PPM hydrogels with the different temperature ranging from 30°C to 50°C. (c, d) SEM images of PPM hydrogel (10,000 magnification and 20,000 magnification). (e) Profile of DS-EVs released from the Ti-PPM composite scaffold. (f-h) NIR thermal images of Ti, Ti-PPM and Ti-PPM-DS-EVs, these implants exposed to an 808 nm (E = 1000 mW/cm^2) laser after 600 s.

(Figure S8). Subsequently, the related protein of Wnt signalling pathway such as wnt3a, β-catenin, phosphorylated β-catenin and GPC6 were detected by Western blot. The results revealed that DS-EVs upregulated the expression of wnt3a, phosphorylated β-catenin and GPC6 in the presence of Ti-PPM wear debris. (Figure 5f,j). Collectively, the above results indicated that DS-EVs may inhibit osteolysis and promote osseointegration in vitro by activating the GPC6/Wnt signalling pathway (Figure 5k).

2.6 | Characterisation of Extended Release of DS-EVs in Ti-PPM Composite Scaffolds

PVA hydrogels are considered as the promising exosomes delivery material due to those temperature sensitive features. PPM hydrogels are stabilised via interchain hydrogen bonds and hydrophobic interactions, whereas an increase in temperature through NIR light regulation gives rise to the dissociation of hydrogen bonds with ensuing dissolution of the hydrogel, enabling the release of EVs (Figure 6a). The swelling ratios of PP and PPM hydrogels were determined in phosphate-buffered Saline (PBS) at pH = 7.4 with the temperature ranging from 30°C to 50°C. As shown in Figure 6b, the swelling ratios of PP and PPM hydrogels increased with the increasing temperature, might be due to the temperature sensitivity of PP hydrogel, which is consistent with previous reports (Byun et al. 1996). Furthermore, in contrast to PP hydrogels, the swelling rate of the PPM hydrogels was reduced, ascribed to the well-dispersed MXene sheet acting as cross-linking points, providing additional physical crosslinking within the covalently cross-linked hydrogel network. After lyophilisation of the hydrogel, the spatial network structure of the PPM hydrogel is shown in Figure 6c,d. The release behaviour of EVs loaded in Ti-PPM was showed in Figure 6e, EVs were controlled released when encapsulated into the Ti-PPM scaffold under the NIR light. Collectively, Ti-PPM scaffold was selected to deliver DS-EVs for the further in vivo experiments. Moreover, the surface temperature of these scaffolds was changed under near-infrared light (Figures 6f-h and S9–S13), and an

20013078, 2025, 6, Downloaded from https://isevjournals.onlinelibrary.wiley.com/doi/10.1002/jev2.70098 by CochraneChina, Wiley Online Library on [23/06/2025]. See the Terms and Conditions (https://onlinelibrary.wiley.com/terms-and-conditions) on Wiley Online Library for rules of use; OA articles are governed by the applicable Creative Commons License

increase in temperature gives rise to the dissociation of hydrogen bonds with ensuing dissolution of the hydrogel.

2.7 | DS-EVs Effectively Promote Bone Regeneration and Osseointegration In Vivo

To further evaluate the efficacy of DS-EVs in treating bone defects in vivo, we surgically established distal femoral bone defects in rats (Figure 7a). The temperature of the Ti-PPM-DS-EVs in vivo increased from 33.3°C to 42°C exposed to an 808 nm (E = 1000 mW/cm^2) laser for 600 s (Figure 7b), providing comfortable conditions for the controlled release of DS-EVs. In order to assess the in vivo bone regeneration efficacy and biocompatibility of DS-EVs, the animals were euthanised at 12 weeks post-surgery, and distal femoral tissues were collected for micro-CT, histological analyses. The reconstructed micro-CT images of the cross-sections of the rat femur with the composite scaffold are shown in Figure 7c. Newly regenerated bone, shown in red in the defect area, was observed in all groups. However, the newly formed bone tissue, which was well-integrated with the surrounding bone tissue, was notably enhanced at the bone-scaffold contact surface in the Ti-PPM-DS-EVs group under NIR light. Moreover, microarchitectural parameters, such as bone volume/tissue volume (BV/TV), trabecular thickness (Tb. Th) and trabecular number (Tb. N) were measured to evaluate the newly regenerated bone tissue (Figure 7d-f). Consistently, the values of BV/TV, Tb. Th and Tb. N in the Ti-PPM-DS-EVs group was significantly higher compared to those in the Ti-PPM-EVs group. The regenerated neotissue partially filled with the drilled defects and appeared irregular around surrounding the bone tissue in the Ti-PPM group and Ti-PPM-EVs group, whereas the neotissue in the Ti-PPM-DS-EVs group revealed intense and continuous red colour, completely integrating with the scaffold (Figure 7g,h). Moreover, the area of newly formed bone tissue stained in the Ti-PPM-DS-EVs (with NIR light) was significantly enhanced compared to Ti-PPM-DS-EVs (without NIR light) group. Collectively, compared to normal EVs, DS-EVs exhibited more favourable stimulatory effect on bone regeneration and osseointegration in vivo.

3 | Discussion

Titanium alloy is a promising scaffold biomaterial for bone tissue engineering. However, the wear debris in the vicinity of bone may give rise to inflammatory osteolysis, resulting in sterile loosening of such implants due to the poor wear resistance of titanium alloy surfaces. In this study, we fabricated chemically tagged DS-EVs to target activated macrophages via MGL-mediated click chemistry. In vitro assays supported the robust role of DS-EVs for the inhibition of osteoclastogenesis via skewing macrophage polarisation, which further promoted the osteogenic differentiation of BMSCs by regulating Wnt/GPC6 signalling pathway. Moreover, we designed the PPM coatings to strengthen the interfacial adhesion and realize the frequency conversion release of EVs through temperature change. In vivo results revealed the favourable function of high-quality intelligent titanium alloy scaffold contained DS-EVs in promoting osseointegration.

The fundamental mechanism of inflammatory osteolysis is believed to be the interaction between macrophages and osteoclasts. The inflammatory cytokines derived from M1 macrophages regulate osteoclast formation and function, performing a potential role in the development of focal osteolysis. Therefore, targeting and repolarising macrophages to the M2 phenotype to block the secretion of inflammatory factors and reduce the activity of the bone-resorptive cells is a promising therapeutic strategy for inflammatory osteolysis. As the critical mediators of intercellular communication, EVs are incrementally accredited as potential cell-free therapeutic nanomedicines. Previous studies have confirmed the favourable properties of MSC-EVs in macrophage polarisation and anti-inflammation (Soufihasanabad et al. 2024; Tang et al. 2024). However, there is still a lack the efficacious procedures for surface-editing EVs to target macrophage cells and enhance polarisation efficiency. MGL is an approach to regulate cellular metabolism and glycosylation, which is universally applicable to drug delivery and immune-targeted therapies (Agatemor et al. 2019). Moreover, MGL approach combined with bioorthogonal click chemistry technology enables efficient cellular surface modification (Yoon et al. 2017). In this study, we aimed to construct an innovative functional EVs-based strategy via MGL-mediated click chemistry. Nevertheless, the therapeutic effect and the underlying mechanism of action of DS-EVs in bone remodelling remain to be investigated.

DS is a specific ligand of SR-A that is an activated macrophage-specific protein. To construct the novel MGL EVs, hUCMSCs were labelled the surface azido groups, which enabled the conjugation of DBCO-DS via efficient click chemistry. Cy5.5-labelled DS was colocalised with CD63 fluorescent signal after the surface engineering of hUCMSCs, suggesting that the surface engineering was successful via MGL-mediated click chemistry. Subsequently, we evaluated the intrinsic biogenesis of the DS-EVs. The fluorescence signal of EFA1, an early endosome marker, was generated and co-localised with Cy5.5-labelled DS in a time-dependent manner, indicating that the newly generated EVs with the DS tag via MGL-mediated click chemistry. Furthermore, DS-EVs revealed little difference compared to normal EVs in terms of their size, shape and morphology, suggesting that MGL-mediated click chemistry did not disrupt the morphology and function of DS-EVs. In addition, DS-EVs exhibited a superior effect in terms of suppressing inflammatory microenvironment, skewing macrophage polarisation from M1 to M2 phenotype, and inhibiting osteoclastogenesis, which helped the prevention of osteolysis. Moreover, DS-EVs promoted the osteogenic differentiation of BMSCs, improving the status of osseointegration. Additionally, DS-EVs reversed the pathological process of osteolysis by upregulating the expression of OPG, an important RANKL decoy receptor that impedes osteoclast maturation and osteoclast bone resorption. Transcriptome profiling was performed to further investigate the underlying mechanism of DS-EVs in osseointegration and osteolysis. We demonstrated that DS-EVs upregulated the expression of Wnt3a, phosphorylated β-catenin and GPC6, activating Wnt/GPC6 signalling pathway to promote osseointegration and suppress osteolysis.

To strengthen the interfacial adhesion and reduce wear between the implants and the bone tissue, we developed an MXene-PVA/AAc composite hydrogel coating for titanium scaffolds,

20013078, 2025, 6, Downloaded from https://isevjournals.onlinelibrary.wiley.com/doi/10.1002/jev2.70098 by CochraneChina, Wiley Online Library on [23/06/2025]. See the Terms and Conditions (https://onlinelibrary.wiley.com/terms-and-conditions) on Wiley Online Library for rules of use; OA articles are governed by the applicable Creative Commons License

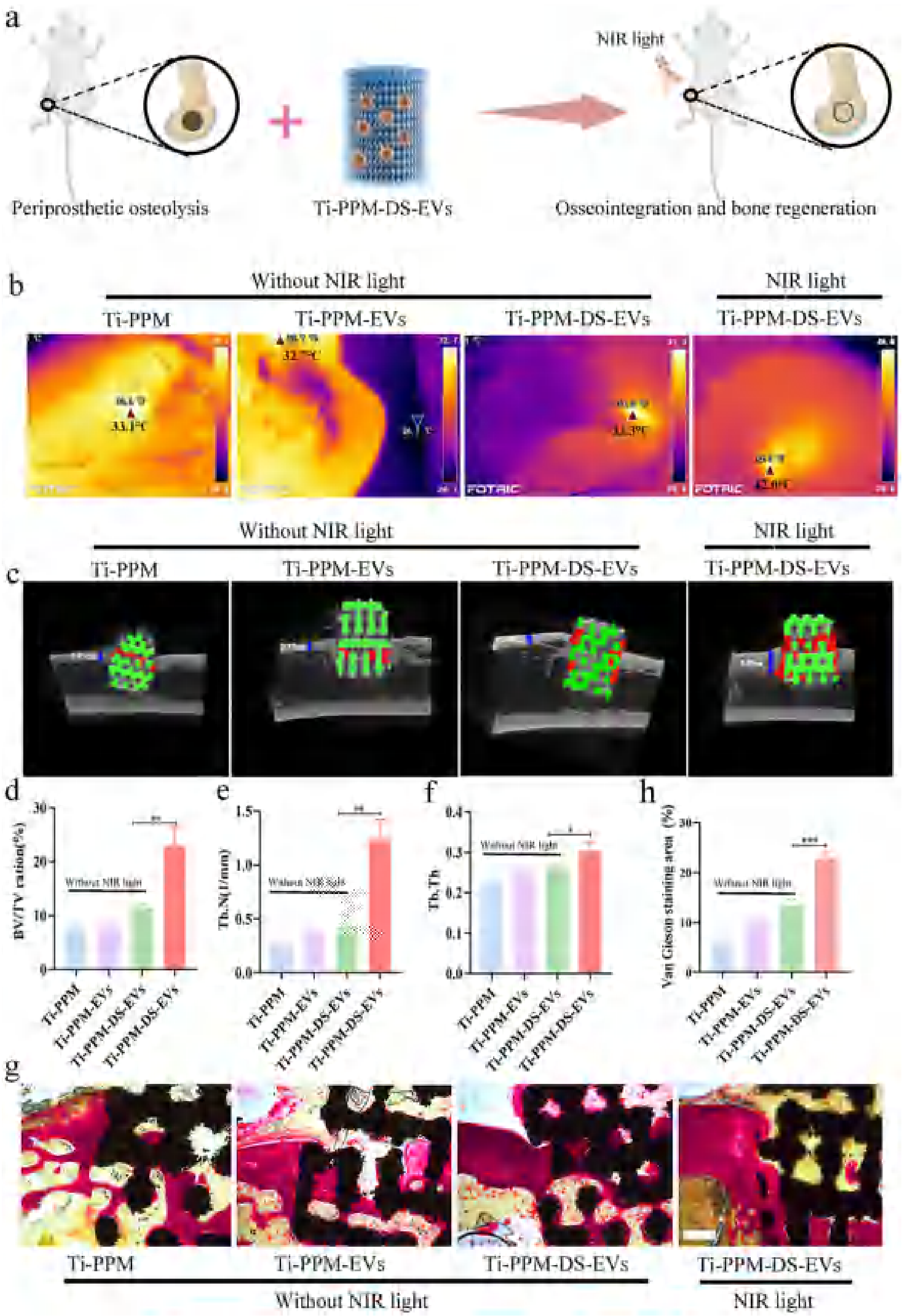

FIGURE 7 | DS-EVs effectively promote osseointegration in vivo. (a) Schematic of femur defect rat model and composited scaffold contained DS-EVs administration. (b) NIR thermal images of the implants exposed to an 808 nm (E = 1000 mW/cm^2) laser after 600 s. (c) Micro-CT images of the rat femurs at 12 weeks postsurgery. (d) Quantitative results of the new bone including bone volume/tissue volume (BV/TV). (e) Quantitative results of trabecular number (Tb.N) and (f) trabecular thickness (Tb.Th). Three independent replicates have been statistical analysis. *$p < 0.05$, **$p < 0.01$, ***$p < 0.001$. (g) Van Gieson's staining of regenerated bone repaired by composited scaffold. Scale bar: 500 µm. (h) Quantitative results of Van Gieson's staining area. ***$p < 0.001$.

20013078, 2025, 6, Downloaded from https://isevjournals.onlinelibrary.wiley.com/doi/10.1002/jev2.70098 by CochraneChina, Wiley Online Library on [23/06/2025]. See the Terms and Conditions (https://onlinelibrary.wiley.com/terms-and-conditions) on Wiley Online Library for rules of use; OA articles are governed by the applicable Creative Commons License

which is referred to as the Ti-PPM composite scaffold. The PVA/AAc hydrogel exhibited excellent anti-wear properties of titanium alloys rubbing against bone due to its dissipation for the interface residual stress (Ji et al. 2024; Wang et al. 2016). MXene, known for its outstanding mechanical properties, photothermal effects, wear resistance and biocompatibility (He et al. 2021; Qu et al. 2023; Zhou et al. 2022), also offers high absorption and photothermal conversion efficiency for near-infrared (NIR) light. Hu et al. reported that the piezoresistive MXene/Silk fibroin nanocomposite hydrogel was able to accelerate bone regeneration (Hu et al. 2023). In this study, we constructed a Ti-PPM composite scaffold to load DS-EVs, achieving the frequency-conversion release of EVs and optimising the therapeutic effect of DS-EVs in vivo. The engineered EVs were steadily released from the coated hydrogel by regulating the pore structure size of thermosensitive PVA-PAA-hydrogel through NIR light irradiation. In vivo results revealed that DS-EVs possess a more promising therapeutic effect for bone defects compared to normal EVs.

In summary, we prepared a novel engineering DS-EVs, which can target macrophages and skew macrophage polarisation from M1 to M2 phenotype, inhibiting osteoclastogenesis and promoting osseointegration through activating GPC6/Wnt signalling pathway in vitro. Additionally, we constructed a multifunctional Ti-PPM composite scaffold, which exhibited desirable wear resistance, excellent interfacial adhesion and achieved the frequency conversion release of EVs, promoting the effects of DS-EVs in osseointegration in vivo. Taken together, DS-EVs possess great potential for regulating osseointegration.

4 | Conclusion

In summary, to enhance the targeting ability to inflammatory osteolysis, we developed a novel engineered DS-EVs using MGL-mediated click chemistry. The targeted delivery of EVs, obtained from metabolically engineered stem cells, offers a novel cell-free therapeutic system for periprosthetic osteolysis. DS-EVs possess the capacity to target macrophages, shifting their polarisation from the pro-inflammatory M1 to the pro-healing M2 phenotype. Inhibiting osteoclastogenesis and promoting osseointegration via activating GPC6/Wnt signalling pathway in vitro. Furthermore, a multifunctional Ti-PPM composite scaffold, incorporating DS-EVs, provides a robust delivery system for treating periprosthetic osteolysis. This system not only offers superior wear resistance and interfacial adhesion but also facilitates the controlled release of EVs, maximising the osseointegration effects of DS-EVs in vivo. Collectively, our findings suggest that DS-EVs have significant potential to revolutionise osseointegration therapy by regulating osseointegration and improving bone implant therapies.

4.1 | Experimental Section

4.1.1 | Synthesis of DBCO-DS

According to the published protocol (You et al. 2021), DS (Sigma, Germany) and DBCO-amine (Click Chemistry Tools, A103-25, USA) were mixed and dissolved in acetate buffer (Sigma, Germany). Subsequently, $NaBH_3CN$ (Tokyo Chemical Industry, Japan) was added into the above mixture and then reacted thoroughly at 50°C. Distilled water/methanol and Distilled water were sequentially used to dialyse the above mixture for 48 h. Finally, the dialysed samples were lyophilised.

4.2 | Metabolic Tagging of hUCMSCs

hUCMSCs at the density of 2×10^4 cells were co-cultured with 20 µmol $Ac_4ManNAz$ in the cell slide on the 24 well plate for 2 days. Then, after washing with Dulbecco's Phosphate-Buffered Saline (DPBS), the treated cells were stimulated with Cy5.5-labelled DBCO-DS in the foetal bovine serum-free medium for 3 h. Subsequently, the supernatant was removed, and the cell were washed with DPBS. After incubated for 24 h, the cells were fixed with 4% paraformaldehyde (PFA). hUCMSCs were treated with 0.25% Triton X-100 and then blocked with 5% donkey serum. Anti-EEA1 and CD63 antibodies were co-incubated with cells overnight at 4°C. In addition, the cells were washed with PBS and then conjugated with a fluorescent secondary antibody (Invitrogen, USA). The nuclei were stained with DAPI at room temperature. The stained cells were visualised under the confocal microscope.

4.3 | Isolation and Identification of DS-EVs

hUCMSCs were incubated with 20 µm $Ac_4ManNAz$ in the basal medium (DAKAWE, 6114021, China) supplemented serum analogue EliteGro-Adv (Elitecell Biomedical, EPA-050, Canada) and 1% Penicillin-Streptomycin Solution (NEST Biotechnology, 211092, China) for 2 days. Subsequently, the treated cells were washed with DPBS and then cultured with Cy5.5-labeled DBCO-DS in the foetal bovine serum-free medium for 3 h. Then, the medium was removed, and basal medium was added. After the 24 h incubation, the conditional medium containing DS-EVs was collected. DS-EVs were isolated via gradient centrifugation. In brief, the conditional medium was centrifuged at 300 g for 10 min, 2000 g for 10 min to remove dead cells. The centrifuge tubes were obtained from PakGent Bioscience. Then, the supernatants were added in a novel ultracentrifuge tube and then centrifuged at 10,000 g for 30 min at 4°C to clear away cell debris. DS-EVs were obtained after centrifugation at a speed of 100,000 g. The size distribution and concentration of DS-EVs were measured by nanoparticle tracking analysis (NTA). The morphology of DS-EVs was observed via transmission electron microscope (TEM).

4.4 | Construction of an Anti-Wear Coating With DS-EVs on the Porous Ti6Al4V Scaffold

The design and fabrication of medical grade porous Ti6Al4V scaffold through 3D printing method were shown in Supporting Information 1.2. Then, the Ti6Al4V scaffolds were pretreated for grafting the transition layer, as exhibited in Supporting Information 1.3. After that, an anti-wear coating with DS-EVs were constructed on the preprocessed scaffolds, as follows. 5 wt% PVA (0.5 g) was dissolved in 10 mL H_2O at 95°C oil baths, the PVA solution was cooled after heating for 30 min. Then, the obtained PVA solution was mixed with 20 wt% acrylic acid (2 g), 0.2 wt% N,N′-methylenebisacrylamide (0.02 g) and 0.5 mol% ammonium persulfate (0.0316 g) dissolved in 10 mL H_2O. After

20013078, 2025, 6, Downloaded from https://isevjournals.onlinelibrary.wiley.com/doi/10.1002/jev2.70098 by CochraneChina, Wiley Online Library on [23/06/2025]. See the Terms and Conditions (https://onlinelibrary.wiley.com/terms-and-conditions) on Wiley Online Library for rules of use; OA articles are governed by the applicable Creative Commons License

mixture uniformly, the MXene (100 ppm) and DS-EVs (20 µg/mL) were added in the above reagents and stirred thoroughly using a magnetic stirrer.

Finally, the 3D titanium alloy with APTES and DA transition layers was fixed on the spined platform and the rotational speed is set to 800 rpm. Subsequently, 0.5 mL of mixed solutions were uniformly dropped onto the titanium alloy, controlling the drip in 15–20 s. Afterwards, the obtained samples were solidified in a 50°C oven, frozen in a refrigerator for 12 h, and then refrigerated and thawed for 12 h, with 2–3 cycles of freezing and thawing. The sample was referred to Ti-PPM-DS-EVs.

4.5 | Osteoclast Differentiation

Trap staining (Sigma, 387A-1KT, USA) was carried out to identify the osteoclast differentiation derived from RAW264.7 mouse cell lines. RAW264.7 mouse cell lines were cultured in RPMI 1640 (Gibco, 11875093, USA) medium supplemented with 10% foetal bovine serum (JYK-FBS-301, Jin Yuan Kang Biotechnology) and 1% penicillin/streptomycin (NEST Biotechnology, 211092, China). As previously described (Zhao et al. 2024), the cells were incubated in the completed medium supplemented with the receptor activator of NF-κB ligand (RANKL, 30 ng/mL), 50 ng/mL of human M-CSF (Peprotech, AF-300-25, USA), EVs or DS-EVs (20 µg/mL) in the 24 well plates. The medium was refreshed every 3 days.

4.6 | ALP Activity Assay

According to the published protocol (Hu et al. 2022), BMSCs were extracted from the bone marrow of 4–6 weeks old female C57BL/6 mice and cultured in α-MEM medium supplied10% foetal bovine serum (Gibco, 10099141, USA) and 1% penicillin and streptomycin. Subsequently, the isolated BMSCs were cultured with Ti-PPM wear debris (2 mg/mL), EVs or DS-EVs (20 µg/mL) in the osteogenic differentiation medium (the basic medium supplied ascorbic acid, 1 µM dexamethasone, glycerol-2-phosphate) for 7 days. At the point time, BMSCs were fixed with 4% paraformaldehyde (PFA) and then incubated with 0.1% Triton X-100 for 10 min. At last, BMSCs were stained with an ALP kit (Sigma, Germany) at 37°C for 30 min.

4.7 | Calcium Deposition Assay

BMSCs were cultured with Ti-PPM wear debris (2 mg/mL), EVs or DS-EVs (20 µg/mL) in the osteogenic differentiation medium (the basic medium supplied ascorbic acid, 1 µM dexamethasone, glycerol-2-phosphate) for 14 days. At the point time, BMSCs were fixed with 4% paraformaldehyde (Procell, China) and then were washed with ddH$_2$O for three times. To evaluate calcium deposition of the differentiated cells, BMSCs were stained with alizarin red stain (ARS, Sigma, Germany) for 10 min.

4.8 | Cell Proliferation Assay

The proliferation of BMSCs stimulated by EVs or DS-EVs was measured by cell counting kit-8 (Sparkjade Biotechnology, China). As described previously (Hu et al. 2020), BMSCs were cultured with EVs or DS-EVs in the presence of Ti-PPM wear debris (2 mg/mL) for 1, 3 and 7 days. At the point time, BMSCs were co-incubated with 10 µL CCK8 for 3 h. The cell viability was investigated using an enzyme linked immunosorbent assay plate reader in by 450 nm absorbance values. Data was presented as mean ± SD of three number of replicates.

4.9 | In Vitro Macrophage Polarisation

RAW264.7 cells were cultured in the RPMI 1640 medium supplemented with 10% FBS, 1% penicillin/streptomycin, 500 ng/mL of LPS in confocal dishes for 24 h. Subsequently, the cells were treated with EVs or DS-EVs (20 µg/mL) for 48 h. Immunofluorescence staining was performed to observe macrophage polarisation in vitro. Briefly, the cells were fixed with 4% PFA and then washed with PBS. After incubating with 0.25% Triton X-10, the cells were blocked with 5% donkey serum. CD206 and iNOS antibodies were co-incubated with cells overnight at 4°C. In addition, the cells were washed with PBS and then conjugated with a fluorescent secondary antibody (Invitrogen, USA). The nuclei were stained with DAPI at room temperature. The stained cells were visualised under the confocal microscope.

4.10 | Western Blot Assay

The cell was lysed by radio-immunoprecipitation assay. The cells were quantified for protein content by BCA protein assay kit. Subsequently, 200,000 µg protein was separated by SDS-PAGE gel (Sparkjade, China) and then transferred to polyvinylidene difluoride (PVDF) membranes. After being blocked by 5% bovine serum albumin (BSA) under gentle shaking for 1 h, the membranes were incubated with the primary antibodies for 12 h. Next, the membranes were washed with tris buffered saline with tween-20(TBST) and then incubated with the second antibodies for 1 h at room temperature. The membranes were scanned using a Tanon 4500. Primary antibodies included anti-β-catenin (CST, 9582, USA), anti-P-β-catenin (CST, 4176, USA), WNT-3a (CST, 2721, USA), anti-osteopontin (Forevertech Biotechnology, P22207, China), Runx-2(CST, 12556, USA), Glypican-6(RD, AF1053, USA), CD9 (Abcam, ab236630, USA), CD81 (Abcam, ab109201, USA), CD63 (Abcam, ab271286, USA), β-actin (Forevertech Biotechnologies, China).

4.11 | Quantitative RT-PCR Analysis

Total RNA isolation was carried out using TRIZOL reagent (YALI Biotech Co., Ltd, YR23014, Jiangsu, China). Cellular RNA Extraction Kit (Accurate Biotechnology (HUNAN) Co., Ltd, Changsha, China) were used to extract RNA. Then, 1000 ng RNA was converted into cDNA using the RevertAid First Strand cDNA Synthesis Kit (Thermo, USA). Subsequently, 10 ng cDNA was added in each well for qPCR reaction. Quantitative Real-Time PCR was carried out with TB Green Premix EX Taq II (Takara,

20013078, 2025, 6, Downloaded from https://isevjournals.onlinelibrary.wiley.com/doi/10.1002/jev2.70098 by CochraneChina, Wiley Online Library on [23/06/2025]. See the Terms and Conditions (https://onlinelibrary.wiley.com/terms-and-conditions) on Wiley Online Library for rules of use; OA articles are governed by the applicable Creative Commons License

RR820A, Japan) and the primers of the osteogenic markers (10 μL TB Green, 0.8 μL primers, 2 μL cDNA, 7.2 μL H_2O) on the ABI Prism 7300 Thermal Cycler (Applied Biosystems, Australia). The primers, including osteocalcin (OCN), alkaline phosphatase (ALP) and bone morphogenetic protein-2 (BMP-2) are shown in Table S1.

4.12 | Ti Alloy Osteolysis Animal Model

Animal management procedures were approved by the Animal Ethics Committee of the First Affiliated Hospital of Naval Medical University (CHECAE2022018) under the guidelines. All surgical procedures were carried out under sterile environment. Sprague-Dawley rats (8 weeks old) were anaesthetised by injecting 4% chloral hydrate (1 mL/100 g), shaved, and disinfected respectively. The skins and the muscles were successively slitted, and the distal femur was partially exposed. Subsequently, bone defect (2 mm in diameter and 1.5 mm in depth) was created in the central area of the femoral shaft by electrical drill. Ti-PPM, Ti-PPM-EVs, Ti-PPM-DS-EVs composite scaffolds were respectively implanted into area of bone defect. Moreover, 6 mg fabricated wear was implanted around the scaffolds to induce osteolysis. The surgical area is irradiated with 808 nm near-infrared light (E = 1000 mW/cm^2) for 600 s every 3 days. At 12 weeks post-operation, all animals were sacrificed by injecting overdose of chloral hydrate.

4.13 | Micro-CT Assay

Micro-computed tomography assessment (micro-CT) of femurs was carried out by Skyscan 1272 to evaluate the new bone formation around the implants after 12 weeks post-surgery. Three-dimensional (3D) images were reconstructed and analysed by Data viewer software. The areas of titanium alloy screws, cortical bone and newly bone were distinguished and marked with three different colours on the micro-CT images. Bone volume fraction (bone volume/tissue volume, BV/TV), trabecular number (Tb.N) and trabecular thickness (Tb.Th) were analysed by CT analysis software.

4.14 | Histomorphometry Observation

The femurs contained the Ti alloy scaffolds were dehydrated using a graded alcohol series, starting at 75% concentration and progressing to 100%, and then immersed in polymethyl methacrylate (PMMA). The embedded samples were sectioned into 150 μm-thick slices using a saw microtome (Leica SP1600, Hamburg, Germany). These sections were then ground and polished to a final thickness of approximately 40 μm. Finally, the mineralised bone tissues were observed under the microscope after staining with van Gieson's solution

4.15 | Statistical Analysis

All data are analysed by GraphPad prism 8 statistical software and presented as mean ± standard deviation. The unpaired student's test was used to compare the differences between two groups. One-way analysis of variance (ANOVA) was used for multiple groups to assess the differences. Differences were considered significant at $p < 0.05$ (*), $p < 0.01$ (**) and $p < 0.001$ (***). Data were presented as the mean ± standard deviation of three replicates. The *t*-test was used to evaluate the mean beta values of each group.

Author Contributions

Chenchen Wang: data curation (equal), investigation (equal), writing–original draft (equal). **Jiang Ju**: data curation (equal), investigation (equal), software (equal). **Chao Fu**: Formal analysis (equal). **Bingbo Bao**:Data Curation (equal). **Tianhui Ren**: conceptualization (equal), formal analysis (equal). **Yanan Li**: investigation (equal). **Yuan Wang**: formal analysis (equal), investigation (equal). **Sheng Han**: conceptualization (equal), writing–review and editing (equal). **Xuan Huang**: funding acquisition (equal), project administration (equal), writing–review and editing (equal). **Hongxing Hu**: Investigation, Writing - Original Draft and Visualization. **Xianyou Zheng**: conceptualization (equal), project administration (equal), writing–review and editing (equal).

Acknowledgement

This work is grateful for the support of the Basic Medical Research Foundation of Naval Medical University (2023PY20, 2023MS022). National Natural Science Foundation of China (Grant 82372388, 82172421). 'Chen-Guang' project (22CGA75) supported by Shanghai Municipal Education Commission and Shanghai 'Science and Technology Innovation Action Plan' Morning Star Cultivation (Sailing Program 22YF1447500) and Collaborative Innovation Center of Fragrance Flavour and Cosmetics.

Conflicts of Interest

The authors declare no conflict of interest.

Data Availability Statement

The data that support the findings of this study are available from the corresponding author upon reasonable request.

References

Abd-Elaziem, W., M. A. Darwish, A. Hamada, and W. M. Daoush. 2024. "Titanium-Based Alloys and Composites for Orthopedic Implants Applications: A Comprehensive Review." *Materials & Design* 241: 112850.

Adams, C. T., C. M. O'Connor, J. R. Young, A. A. Anoushiravani, B. S. Doherty, and F. Congiusta. 2021. "Outcomes of a Total Joint Arthroplasty Enhanced Recovery Program in a Community Hospital Setting." *Journal of Arthroplasty* 36, no. 7: S173–S178.

Agatemor, C., M. J. Buettner, R. Ariss, K. Muthiah, C. T. Saeui, and K. J. Yarema. 2019. "Exploiting Metabolic Glycoengineering to Advance Healthcare." *Nature Reviews Chemistry* 3, no. 10: 605–620.

Alquraini, A., and J. El Khoury. 2020. "Scavenger Receptors." *Current Biology* 30, no. 14: R790–R795.

An, J. X., Z. Y. Han, Y. T. Qin, C. X. Li, J. L. He, and X. Z. Zhang. 2024. "Bacteria-Based Backpacks to Enhance Adoptive Macrophage Transfer Against Solid Tumors." *Advanced Materials* 36, no. 6: e2305384.

Bhatta, R., J. Han, Y. S. Liu, et al. 2023. "Metabolic Tagging of Extracellular Vesicles and Development of Enhanced Extracellular Vesicle Based Cancer Vaccines." *Nature Communications* 14, no. 1: 8047.

Byun, J. G., Y. M. Lee, and C. S. Cho. 1996. "Swelling of Thermosensitive Interpenetrating Polymer Networks Composed of Poly(vinyl alcohol) and Poly(acrylic acid)." *Journal of Applied Polymer Science* 61, no. 4: 697–702.

20013078, 2025, 6, Downloaded from https://isevjournals.onlinelibrary.wiley.com/doi/10.1002/jev2.70098 by CochraneChina, Wiley Online Library on [23/06/2025]. See the Terms and Conditions (https://onlinelibrary.wiley.com/terms-and-conditions) on Wiley Online Library for rules of use; OA articles are governed by the applicable Creative Commons License

Canalis, E. 2013. "Wnt Signalling in Osteoporosis: Mechanisms and Novel Therapeutic Approaches." *Nature Reviews Endocrinology* 9, no. 10: 575–583.

Capurro, M., T. Izumikawa, P. Suarez, et al. 2017. "Glypican-6 Promotes the Growth of Developing Long Bones by Stimulating Hedgehog Signaling." *Journal of Cell Biology* 216, no. 9: 2911–2926.

Chen, C. J., J. K. Li, Y. Yang, et al. 2023. "Enhanced Recovery After Total Joint Arthroplasty (TJA): A Contemporary Systematic Review of Clinical Outcomes and Usage of Key Elements." *Orthopaedic Surgery* 15, no. 5: 1228–1240.

Chen, L. J., K. Peng, H. Huang, et al. 2024. "Injectable Hydrogel Based on Enzymatic Initiation of Keratin Methacrylate for Controlled Exosome Release in Intervertebral Disc Degeneration Therapy." *Advanced Functional Materials* 34, no. 32: 2316545.

Drees, P., A. Eckardt, R. E. Gay, S. Gay, and L. C. Huber. 2007. "Mechanisms of Disease: Molecular Insights Into Aseptic Loosening of Orthopedic Implants." *Nature Clinical Practice Rheumatology* 3, no. 3: 165–171.

Feng, Z. Y., Z. Jing, Q. Li, et al. 2023. "Exosomal STIMATE Derived From Type II Alveolar Epithelial Cells Controls Metabolic Reprogramming of Tissue-Resident Alveolar Macrophages." *Theranostics* 13, no. 3: 991–1009.

Gao, Y. S., C. L. Dai, M. Zhang, et al. 2023. "Biomimetic Silk Fibroin Hydrogel for Enhanced Peripheral Nerve Regeneration: Synergistic Effects of Graphene Oxide and Fibroblast Exosome." *Advanced Functional Materials* 34, no. 17: 2314610.

Goodman, S. B., P. Huie, Y. Song, et al. 1998. "Cellular Profile and Cytokine Production at Prosthetic Interfaces—Study of Tissues Retrieved From Revised Hip and Knee Replacements." *Journal of Bone and Joint Surgery. British Volume* 80, no. 3: 531–539.

Groenbaek, H., S. Rodgaard-Hansen, N. K. Aagaard, et al. 2015. "The Macrophage Activation Markers Soluble Cd206 and Cd163 Predict Mortality in Patients With Liver Cirrhosis and Acute-on-Chronic Liver Failure (Aclf)." *Journal of Hepatology* 62: S274–S274.

Han, M., H. R. Yang, X. D. Lu, et al. 2022. "Three-Dimensional-Cultured MSC-Derived Exosome-Hydrogel Hybrid Microneedle Array Patch for Spinal Cord Repair." *Nano Letters* 22, no. 15: 6391–6401.

Hansen, M. S., K. Madsen, M. Price, et al. 2024. "Transcriptional Reprogramming During Human Osteoclast Differentiation Identifies Regulators of Osteoclast Activity." *Bone Research* 12, no. 1: 5.

Hascoët, E., F. Blanchard, C. Blin-Wakkach, J. Guicheux, P. Lesclous, and A. Cloitre. 2023. "New Insights Into Inflammatory Osteoclast Precursors as Therapeutic Targets for Rheumatoid Arthritis and Periodontitis." *Bone Research* 11, no. 1: 26.

He, D. M., M. Cai, H. Yan, et al. 2021. "Tribological Properties of Ti3C2Tx MXene Reinforced Interpenetrating Polymers Network Coating." *Tribology International* 163: 107196.

Hu, H., Z. Wang, H. Yang, Y. Bai, R. Zhu, and L. Cheng. 2023. "Hypoxic Preconditional Engineering Small Extracellular Vesicles Promoted Intervertebral Disc Regeneration by Activating Mir-7-5p/NF-Kappab/Cxcl2 Axis." *Advanced Science (Weinheim)* 10, no. 35: e2304722.

Hu, H. X., L. L. Dong, Z. H. Bu, et al. 2020. "miR-23a-3p-Abundant Small Extracellular Vesicles Released From Gelma/Nanoclay Hydrogel for Cartilage Regeneration." *Journal of Extracellular Vesicles* 9, no. 1: 1778883.

Hu, H. X., H. Zhang, Z. H. Bu, et al. 2022. "Small Extracellular Vesicles Released From Bioglass/Hydrogel Scaffold Promote Vascularized Bone Regeneration by Transferring miR-23a-3p." *International Journal of Nanomedicine* 17: 6201–6220.

Hu, Z. C., J. Q. Lu, T. W. Zhang, et al. 2023. "Piezoresistive MXene/Silk Fibroin Nanocomposite Hydrogel for Accelerating Bone Regeneration by Re-Establishing Electrical Microenvironment." *Bioactive Materials* 22: 1–17.

Jafarigol, E., M. B. Salehi, and H. R. Mortaheb. 2021. "Synergetic Effects of Additives on Structural Properties of Acrylamide-Based Hydrogel." *Journal of Dispersion Science and Technology* 42, no. 6: 910–919.

Ji, D. C., Z. B. Zhang, J. X. Sun, et al. 2024. "Strong, Tough, and Biocompatible Poly(vinyl alcohol)-Poly(vinylpyrrolidone) Multiscale Network Hydrogels Reinforced by Aramid Nanofibers." *ACS Applied Materials & Interfaces* 16, no. 19: 25304–25316.

Jiang, Y. P., T. H. Jia, W. M. Gong, P. H. Wooley, and S. Y Yang. 2013. "Titanium Particle-Challenged Osteoblasts Promote Osteoclastogenesis and Osteolysis in a Murine Model of Periprosthestic Osteolysis." *Acta Biomaterialia* 9, no. 7: 7564–7572.

Kalluri, R., and V. S. LeBleu. 2020. "The Biology, Function, and Biomedical Applications of Exosomes." *Science* 367, no. 6478: 640.

Kitaura, H., A. Marahleh, F. Ohori, et al. 2020. "Osteocyte-Related Cytokines Regulate Osteoclast Formation and Bone Resorption." *International Journal of Molecular Sciences* 21, no. 14: 1175.

Li, B., Y. Han, and M. Li. 2016. "Enhanced Osteoblast Differentiation and Osseointegration of a Bio-Inspired HA Nanorod Patterned Pore-Sealed MgO Bilayer Coating on Magnesium." *Journal of Materials Chemistry B* 4, no. 4: 683–693.

Liang, Y. J., X. Xu, X. F. Li, et al. 2020. "Chondrocyte-Targeted MicroRNA Delivery by Engineered Exosomes Toward a Cell-Free Osteoarthritis Therapy." *ACS Applied Materials & Interfaces* 13, no. 49: 59591–59591.

Liao, W. Z., C. Ni, R. Y. Ge, et al. 2024. "Nel-Like Molecule Type 1 Combined With Gold Nanoparticles Modulates Macrophage Polarization, Osteoclastogenesis, and Oral Microbiota in Periodontitis." *ACS Applied Materials & Interfaces* 16, no. 7: 8442–8458.

Liu, J. J., B. Zhou, Y. L. Guo, et al. 2021. "SR-A-Targeted Nanoplatform for Sequential Photothermal/Photodynamic Ablation of Activated Macrophages to Alleviate Atherosclerosis." *ACS Applied Materials & Interfaces* 13, no. 25: 29349–29362.

Marquardt, L. M., V. M. Doulames, A. T. Wang, et al. 2020. "Designer, Injectable Gels to Prevent Transplanted Schwann Cell Loss During Spinal Cord Injury Therapy." *Science Advances* 6, no. 14: eaaz1039.

Nielsen, M. C., R. H. Gantzel, J. Clària, J. Trebicka, H. J. Moller, and H. Gronbæk. 2020. "Macrophage Activation Markers, CD163 and CD206, in Acute-on-Chronic Liver Failure." *Cells-Basel* 9, no. 5: 1175.

Overmann, A. L., C. Aparicio, J. T. Richards, et al. 2020. "Orthopaedic Osseointegration: Implantology and Future Directions." *Journal of Orthopaedic Research* 38, no. 7: 1445–1454.

Pedersen, S. L., T. H. Huynh, P. Pöschko, et al. 2020. "Remotely Triggered Liquefaction of Hydrogel Materials." *American Chemical Society Nano* 14, no. 7: 9145–9155.

Qu, X. Y., Y. Guo, C. X. Xie, S. H. Li, Z. Q. Liu, and B. Lei. 2023. "Photoactivated MXene Nanosheets for Integrated Bone-Soft Tissue Therapy: Effect and Potential Mechanism." *American Chemical Society Nano* 17, no. 8: 7229–7240.

Simonet, W. S., D. L. Lacey, C. R. Dunstan, et al. 1997. "Osteoprotegerin: A Novel Secreted Protein Involved in the Regulation of Bone Density." *Cell* 89, no. 2: 309–319.

Soufihasanabad, S., M. Mahmoudi, M. Taghavi-Farahabadi, et al. 2024. "In Vivo Polarization of M2 Macrophages by Mesenchymal Stem Cell-Derived Extracellular Vesicles: A Novel Approach to Macrophage Polarization and Its Potential in Treating Inflammatory Diseases." *Medical Hypotheses* 187: 111353.

Tang, J. D., X. Y. Wang, X. Lin, and C. Wu. 2024. "Mesenchymal Stem Cell-Derived Extracellular Vesicles: A Regulator and Carrier for Targeting Bone-Related Diseases." *Cell Death Discovery* 10, no. 1: 212.

Udagawa, N., M. Koide, M. Nakamura, et al. 2021. "Osteoclast Differentiation by RANKL and OPG Signaling Pathways." *Journal of Bone and Mineral Metabolism* 39, no. 1: 19–26.

20013078, 2025, 6, Downloaded from https://isevjournals.onlinelibrary.wiley.com/doi/10.1002/jev2.70098 by CochraneChina, Wiley Online Library on [23/06/2025]. See the Terms and Conditions (https://onlinelibrary.wiley.com/terms-and-conditions) on Wiley Online Library for rules of use; OA articles are governed by the applicable Creative Commons License

Vlashi, R., X. E. Zhang, M. R. Wu, and G. Q. Chen. 2023. "Wnt Signaling: Essential Roles in Osteoblast Differentiation, Bone Metabolism and Therapeutic Implications for Bone and Skeletal Disorders." *Genes & Diseases* 10, no. 4: 1291–1317.

Wang, C. C., G. Q. Zhang, Z. P. Li, et al. 2019. "Tribological Behavior of Ti-6Al-4 V Against Cortical Bone in Different Biolubricants." *Journal of the Mechanical Behavior of Biomedical Materials* 90: 460–471.

Wang, H., and D. J. Mooney. 2020. "Metabolic Glycan Labelling for Cancer-Targeted Therapy." *Nature Chemistry* 12, no. 12: 1102–1114.

Wang, H., R. B. Wang, K. M. Cai, et al. 2017. "Selective Metabolic Cell-Labeling-Mediated Cancer Targeting." *Nature Chemical Biology* 13, no. 4: 415.

Wang, H., R. B. Wang, K. M. Cai, et al. 2017. "Selective Metabolic Cell-Labeling-Mediated Cancer Targeting." *Nature Chemical Biology* 13, no. 4: 415.

Wang, Q. G., X. Zhou, J. X. Zeng, and J. Z. Wang. 2016. "Water Swelling Properties of the Electron Beam Irradiated PVA-g-AAc Hydrogels." *Nuclear Instruments and Methods in Physics Research Section B: Beam Interactions with Materials and Atoms* 368: 90–95.

Wang, Y., P. P. Tian, H. Cao, et al. 2024. "Improved Corrosion Resistance and Tribological Properties of MXene/NCDs Coatings on the Ti6Al4V Alloys." *Wear* 558-559: 205540.

Wu, Y., J. P. Zitelli, K. S. TenHuisen, X. J. Yu, and M. R. Libera. 2011. "Differential Response of Staphylococci and Osteoblasts to Varying Titanium Surface Roughness." *Biomaterials* 32, no. 4: 951–960.

Yang, J., X. F. Huang, Q. Yu, et al. 2024. "Extracellular Vesicles Derived From M2-Like Macrophages Alleviate Acute Lung Injury in a miR-709-Mediated Manner." *Journal of Extracellular Vesicles* 13, no. 4: e12437.

Yin, N., Y. Z. Zhao, C. H. Liu, et al. 2022. "Engineered Nanoerythrocytes Alleviate Central Nervous System Inflammation by Regulating the Polarization of Inflammatory Microglia." *Advanced Materials* 34, no. 27: e2201322.

Yoon, H. Y., H. Koo, K. Kim, and I. C. Kwon. 2017. "Molecular Imaging Based on Metabolic Glycoengineering and Bioorthogonal Click Chemistry." *Biomaterials* 132: 28–36.

You, D. G., G. T. Lim, S. Kwon, et al. 2021. "Metabolically Engineered Stem Cell-Derived Exosomes to Regulate Macrophage Heterogeneity in Rheumatoid Arthritis." *Science Advances* 7, no. 23: eabe0083.

Zhao, Y., J. Y. Ning, H. Q. Teng, et al. 2024. "Long Noncoding RNA Malat1 Protects Against Osteoporosis and Bone Metastasis." *Nature Communications* 15, no. 1: 2384.

Zhou, Y. J., M. Liu, Y. L. Wang, J. Y. Yuan, and X. H. Men. 2022. "Significance of Constructed MXene@Ag Hybrids for Enhancing the Mechanical and Tribological Performance of Epoxy Composites." *Tribology International* 165: 107328.

Zhou, Z., W. K. Jiang, J. J. Yan, et al. 2023. "Trichostatin A Enhances the Titanium Rods Osseointegration in Osteoporotic Rats by the Inhibition of Oxidative Stress Through Activating the AKT/Nrf2 Pathway." *Scientific Reports* 13, no. 1: 22967.

Supporting Information

Additional supporting information can be found online in the Supporting Information section.

20013078, 2025, 6, Downloaded from https://isevjournals.onlinelibrary.wiley.com/doi/10.1002/jev2.70098 by CochraneChina, Wiley Online Library on [23/06/2025]. See the Terms and Conditions (https://onlinelibrary.wiley.com/terms-and-conditions) on Wiley Online Library for rules of use; OA articles are governed by the applicable Creative Commons License